

A Microwave Scattering Model for Layered Vegetation

N93-18074

Mostafa A. Karam, *Senior Member, IEEE*, Adrian K. Fung, *Fellow, IEEE*,
Roger H. Lang, *Fellow, IEEE*, and Narinder S. Chauhan, *Member, IEEE*

Abstract—A microwave scattering model has been developed for layered vegetation based on an iterative solution of the radiative transfer equation up to the second order to account for multiple scattering within the canopy and between the ground and the canopy. The model is designed to operate over a wide frequency range for both deciduous and coniferous forest and to account for the branch size distribution, leaf orientation distribution, and branch orientation distribution for each size. The canopy is modeled as a two-layered medium above a rough interface. The upper layer is the crown containing leaves, stems, and branches. The lower layer is the trunk region modeled as randomly positioned cylinders with a preferred orientation distribution above an irregular soil surface. Comparisons of this model with measurements from deciduous and coniferous forests show good agreements at several frequencies for both like and cross polarizations. Major features of the model needed to realize the agreement include allowance for (1) branch size distribution, (2) second-order effects, and (3) tree component models valid over a wide range of frequencies.

I. INTRODUCTION

NATURAL phenomena such as the atmospheric carbon dioxide concentration, the hydrologic cycle, and the energy balance in the biosphere are related to the forest. Hence accurate and timely measurements of the forest structure and type through remote sensing are of interest [1]. Of the many ways to measure forest properties, microwave remote sensing is one way which is independent of both weather conditions and the time of day when the measurements can be acquired [2, Chapter 1]. The analysis of these measured data could yield biophysical characteristics of the forest [3]–[5] or its components such as leaves, branches, and trees [6]–[8].

In parallel to the experimental studies, scattering models have been developed to interpret the collected data [9]–[24].

Manuscript received September 19, 1991; revised February 20, 1992.

The work of the first two authors was supported by the National Aeronautics and Space Administration under Grant NAGW-2344 and under NASA's SIR-C data analysis program which is funded through the Jet Propulsion Laboratory.

The work of the last two authors was supported by NASA Grant NAGW-2071 and the NASA EOS Synergism Study organized by JoBea Way of NASA JPL. The numerical evaluations were supported by the Center for High Performance Computing of the University of Texas System.

M. A. Karam and A. K. Fung are with the Wave Scattering Research Center, Electrical Engineering Department, University of Texas at Arlington, Arlington, TX 76019.

R. H. Lang is with the Department of Electrical Engineering and Computer Science, The George Washington University, Washington, DC 20052.

N. S. Chauhan is with the Laboratory for Hydrospheric Processes, Code 974, NASA/Goddard Space Flight Center, Greenbelt, MD 20771.

IEEE Log Number 9200985.

These models may be divided into two categories: i) phenomenological models and ii) physical models.

The phenomenological models are based upon an intuitive understanding of the relative importance of different forest components. Then a scattering model is constructed by summing up the contributions from forest components believed to be important [10]–[12]. The physical models are based upon the interaction of electromagnetic waves with the forest canopy. A canopy can be modeled either as a discrete or a continuous inhomogeneous medium. As a discrete medium the canopy is treated as a collection of randomly distributed discrete scatterers assuming average sizes and shapes of various forest components [13]–[23]. These scatterers may be embedded in one or two layers or a half space medium. For continuous medium modeling, the canopy is treated as a continuous medium with a fluctuating permittivity function [24]. The radiative transfer theory [13]–[20], the distorted Born approximation [21], [22], or the Monte Carlo technique [23] have been used to study electromagnetic interaction with discrete media. The first-order Born and renormalization methods have been applied to study wave scattering from continuous media [24].

Most of the existing scattering models are restricted by assumptions regarding the shape of the scatterers [15]–[21] or the applicable frequency [9], [17]. Some models account only for leaves but not branches or vice versa [16]–[21] and others treat branches and soil surfaces but not leaves [18]. In all these models the scatterers were embedded in one layer above the soil interface or a half space medium.

Recently, a two-layer phenomenological model has been proposed by Richard *et al.* [1987] for a coniferous forested canopy at L-band [11]. In this model the foliage is represented by a cloud of water droplets and the trunk-ground interaction is modeled by dihedral corner reflectors. To avoid issues of tractability and complexity, the individual scattering mechanisms within the forested canopy were modeled separately utilizing empirical or analytical description as appropriate. This model is simple but its domain of applicability is limited. Durden *et al.* [1989] improved this model by replacing the dihedral corner reflector by a finite-length cylinder over a rough interface. The branches are modeled by a layer of randomly oriented cylinders [12]. Several scattering mechanisms are identified and the corresponding Stokes matrices were calculated. The Stokes parameter matrices were then combined to give the total Stokes matrix and resulting polarization signature. The leaf effect was not taken into consideration.

Ulaby *et al.* [1990] proposed a two-layer physical model based on the first-order solution of the radiative transfer theory [13]. This model was used [14], [15] to model multiangle and temporal backscatter from a walnut orchard. It involves the following assumptions:

1. The contribution from trunks in the backscattering direction can be ignored and trunk-ground interaction can be accounted for by considering reflections from the trunks and a flat ground.
2. The cross-polarized term in the trunk phase matrix has been ignored.
3. In the canopy-ground interaction calculation, the ground can be taken to be a specular surface.
4. The forward scattering theorem (optical theorem) can be applied to calculate the extinction coefficient within the canopy. This theorem is accurate to the extent the field scattering amplitude is accurate. Under low frequency approximations this theorem can only provide the loss due to absorption [25]. Hence, scattering loss is not included.
5. The physical optics approach is used to calculate scattering from a leaf. Thus, only leaves larger than a wavelength are considered.

In view of the current status in forest scattering models, there is room for further generalization. The aim of the present study is to develop a scattering model with a wider range of applicability than those available in the literature. In particular, we want to develop a fairly complete but simple physical model which can be applied to both deciduous and coniferous forest over a wide range of frequencies by

1. including coherent and incoherent surface scattering in computation of canopy-soil interactions,
2. using a leaf scattering model which holds for leaves smaller or comparable to the wavelength,
3. accounting for the various branch sizes and their orientation distributions,
4. accounting for cross polarized scattering due to the trunk-ground interactions,
5. using an extinction formulation which accounts for both ohmic and scattering losses where low frequency approximation is made.
6. including the second order radiative transfer solution to account for multiple scattering within the canopy.

A description of the scattering model for a forest canopy is given in Section II. For a linearly polarized incident wave, the explicit expressions for the bistatic scattering coefficient associated with different scattering mechanisms discussed in Section II are given in Section III. In like polarization the second-order volume scattering is generally small compared with the first. However, in cross polarization second-order contribution can be important. Hence, the second-order volume scattering term due to the crown layer is also given.

As a test for the present model comparisons are made between the measured and the predicted values of the backscattering coefficients from both walnut and cypress trees [4], [26]. Two of the authors, Lang and Chauhan have participated in the collection of the walnut tree geometry and ground truth [26].

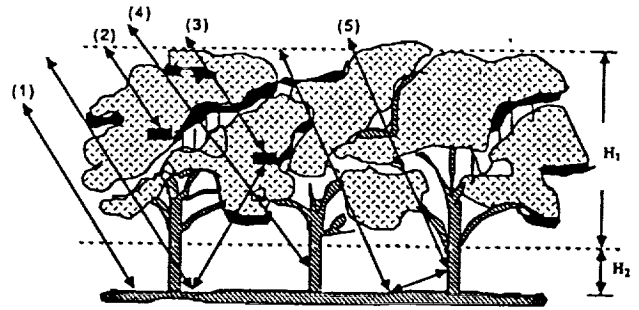


Fig. 1. Geometry of a forest canopy and the backscattering processes for the zero and first-order solutions of the radiative transfer equation: (1) zero order, (2) crown scattering, (3) crown-ground interaction, (4) trunk scattering, (5) trunk-ground interaction.

The cypress tree ground truth is available in the literature [4]. Hence, arbitrary choices of most of the model parameters are avoided.

II. FOREST SCATTERING MODEL DESCRIPTION

The geometry of the scattering problem is given in Fig. 1. It consists of a crown layer and a trunk layer above an irregular surface. Within the crown layer the branches are grouped into different sizes each with an orientation distribution. They are modeled as randomly oriented finite-length dielectric cylinders. The scattering matrix (S matrix) for such cylinders can be obtained by estimating the inner field by that of corresponding infinite cylinder [18]. The validity of this approach for calculating the branch scattering matrix was verified experimentally for branches having length to diameter ratio greater than 5 [27], [28]. The extinction coefficient for the branch model is obtained via the forward scattering theorem since the model does not use low frequency approximation [18]. The deciduous leaves are modeled as randomly oriented circular discs. The coniferous leaves and the stems are modeled as randomly oriented needles. The scattering matrix for a needle or a disc is obtained by applying the Generalized Rayleigh-Gans approximation. This approximation holds for thin leaves and for leaf surface dimension smaller or comparable to the wavelength [27]. Thus, for leaves the extinction coefficients are calculated by summing both the absorption and the scattering coefficients [29]. In summary, the crown layer consists of several groups of scatterers, namely, the leaves and a few different sizes of branches. Scatterers belonging to the same group are identical in size.

Each group of scatterers within the crown layer is a collection of identical scatterers with number density $n_m(m^{-3})$ and a probability density function $P_m(a, h, \alpha, \beta)$ where " a " and " $2h$ " are the radius and length or thickness of a scatterer within the m th group. The angles α and β are the scatterer azimuthal and inclination angles, respectively (Fig. 2). In this study the polar coordinates are used to describe the scatterer orientation with respect to the reference frame and the radial coordinate is parallel to the scatterer axis of symmetry. All the crown constituents are taken to be uniformly oriented in the azimuthal direction. Consequently, the probability density function for the scatterers within the m th group reduces to

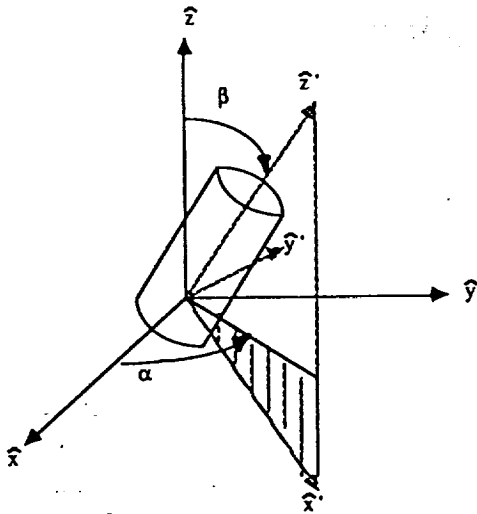


Fig. 2. The polar angles of orientation (defined with respect to the reference frame).

the form,

$$P_m(a, h, \alpha, \beta) = \frac{1}{2\pi} P_m(a, h, \beta). \quad (1)$$

Similarly, the trunk layer may also have several groups of scatterers. Each group is modeled by randomly positioned and vertically oriented identical cylinders with number density $n_m(m^{-3})$. Each group has its own orientation distribution function. Since a trunk can also be modeled as a dielectric cylinder, the scattering amplitude matrix is the same as the branches [18] and so is the representation for the extinction coefficient.

The Kirchhoff model under the scalar approximation is used to represent the scattering properties of the rough soil surface [2]. The surface correlation function is taken to be a Gaussian function with variance σ^2 and correlation length, L .

III. THE BISTATIC SCATTERING COEFFICIENTS

Consider a plane wave incident in $\hat{i}(\pi - \theta_i, \phi_i)$ direction with electric field polarized along \hat{q} direction,

$$\vec{E}_i(\vec{r}) = \hat{q} E_0 e^{-jk \cdot \vec{r}} \quad j = \sqrt{-1} \quad (2)$$

where k is the background medium wavenumber; $\hat{q} = \hat{v}_i$ or \hat{h}_i ; which are the polarization unit vectors (Fig. 3) defined as follows:

$$\begin{aligned} \hat{i} &= \sin \theta_i (\hat{x} \cos \phi_i + \hat{y} \sin \phi_i) - \hat{z} \cos \theta_i \\ \hat{h}_i &= \frac{\hat{z} \times \hat{i}}{|\hat{z} \times \hat{i}|} = \hat{y} \cos \phi_i - \hat{x} \sin \phi_i \\ \hat{v}_i &= \hat{h}_i \times \hat{i} = -\cos \theta_i (\hat{x} \cos \phi_i + \hat{y} \sin \phi_i) - \hat{z} \sin \theta_i. \end{aligned} \quad (3)$$

For the incident field given in (2) and using the albedo as an iteration parameter, the bistatic scattering coefficient from the canopy in $\hat{s}(\theta_s, \phi_s)$ direction can be written as [Appendix A]

$$\sigma_{pq} = \sum_{v=0}^{\infty} \sigma_{pq}^v. \quad (4)$$

In (4) v is the order of the iterative solution of the radiative transfer equation. In the following sections we will consider

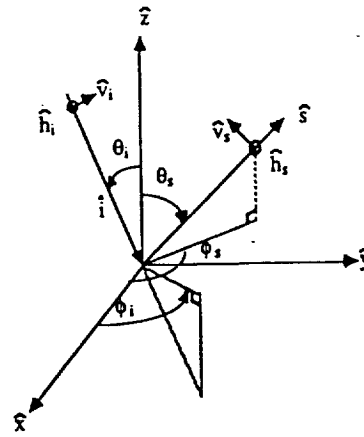


Fig. 3. The polarization vectors of the incident and scattered fields.

the zero, the first, and the second-order contribution to the bistatic scattering coefficient.

A. The Zero-Order Solution (Ground Scattering)

The zero-order solution of the radiative transfer equation is due to ground scattering as illustrated in the backscattering direction by 1 in Fig. 1. The bistatic scattering coefficient of the ground can be written as

$$\sigma_{pq}^0 = L_{1p}(\theta_s) L_{2p}(\theta_s) \sigma_{pq}^s(\theta_s, \phi_s; \pi - \theta_i, \phi_i) L_{2q}(\theta_i) L_{1q}(\theta_i) \quad (5)$$

where $\sigma_{pq}^s(\theta_s, \phi_s; \pi - \theta_i, \phi_i)$ is the pq element of the surface bistatic scattering coefficient matrix given in [2, Chapter 13, pp. 1085–1200]. Its explicit expression depends on the surface parameters and the approximation used to derive it. For a plane interface $\sigma_{pq}^s(\theta_s, \phi_s; \pi - \theta_i, \phi_i)$ reduces to Fresnel reflectivity [2, Chapter 12]. $L_{1q}(\theta_i)$ and $L_{2q}(\theta_i)$ are the q polarized crown and the trunk attenuation factors in the incident direction,

$$L_{tq}(\theta_i) = \exp[-k_{tq}(\theta_i) H_t \sec \theta_i] \quad (t = 1, 2) \quad (6)$$

where $k_{1q}(\theta_i)$ and $k_{2q}(\theta_i)$ are the crown and trunk layer extinction coefficients, respectively [18], [29]. H_1 and H_2 are the heights of the crown and trunk layers. Similar definitions apply to $L_{1p}(\theta_s)$ and $L_{2p}(\theta_s)$ in the scattering direction. The extinction coefficient within the crown region can be written as

$$k_{1p}(\theta_i) = \sum_{m=1}^{N_1} n_m \langle \kappa_{mp}(\theta_i) \rangle \quad (7)$$

where N_1 is the number of groups within the crown layer and $\kappa_{mp}(\theta_i)$ is the extinction cross section for a scatterer within the m th group [18], [29]. The ensemble average $\langle \rangle$ in (7) is taken over the m th group orientation distribution in the following manner:

$$\langle \kappa_{mp}(\theta_i) \rangle = \frac{1}{2\pi} \int d\beta \int d\alpha P_m(\alpha, \beta) \kappa_{mp}(\theta_i). \quad (8)$$

For a discrete probability density function, the integration in (8) reduces to a summation.

Within the trunk layer the extinction coefficient is

$$k_{2p}(\theta_i) = \sum_{m=1}^{N_2} n_m \langle \kappa_{mp}(\theta_i) \rangle \quad (9)$$

where N_2 is the group number within the trunk layer, and $\kappa_{mp}(\theta_i)$ is the extinction cross section for a scatterer within the m th group. The ensemble average in (9) is defined in a way similar to the ensemble average in (8) but with density function describing the trunk orientation distribution.

The backscattering coefficient associated with ground scattering can be obtained from (5) by letting $\theta_s = \theta_i$ and $\phi_s = \phi_i + \pi$, i.e., $\hat{s} = -\hat{i}$.

B. First-Order Solution (Crown and Trunk Scattering)

The first-order solution of the radiative transfer equation leads to a bistatic scattering coefficient in the form

$$\sigma_{pq}^1 = \sigma_{pq}(c) + \sigma_{pq}(c \leftrightarrow g) + \sigma_{pq}(t) + \sigma_{pq}(t \leftrightarrow g). \quad (10)$$

The first term in (10) accounts for crown scattering, the second term for the crown-ground interaction, and the last two terms for the trunk and the trunk-ground scattering, respectively. In the following subsections explicit expressions for those terms will be given along with the physical meaning of each term.

1) *The Crown Scattering*: The bistatic coefficient of the crown is (illustrated in the backscattering direction by 2 in Fig. 1):

$$\sigma_{pq}(c) = 4\pi Q_{1pq}(\theta_s, \phi_s; \pi - \theta_i, \phi_i) \cdot \left\{ \frac{1 - L_{1p}(\theta_s)L_{1q}(\theta_i)}{k_{1p}(\theta_s) \sec \theta_s + k_{1q}(\theta_i) \sec \theta_i} \right\} \quad (11)$$

$$Q_{1pq}(\theta_s, \phi_s; \pi - \theta_i, \phi_i) = \sum_{m=1}^{N_1} n_m \langle |F_{mpq}(\hat{s}, \hat{i})|^2 \rangle$$

where $F_{mpq}(\hat{s}, \hat{i})$ is the element of the scattering amplitude matrix for a scatterer within the m th group [18], [29]. The ensemble average $\langle \rangle$ is taken in a way similar to (8). In (11) the quantity $Q_{1pq}(\theta_s, \phi_s; \pi - \theta_i, \phi_i)$ represents scattering from a unit volume within the crown region. The quantity within the bracket is the resultant of the integration of the loss factor, $\exp[(k_{1p}(\theta_i) \sec \theta_i + k_{1q}(\theta_s) \sec \theta_s)z]$, associated with a unit volume located at z over the crown depth (note that z is negative within the crown region).

The backscattering coefficient is a special case of (11) when we let $\hat{s} = -\hat{i}$. From (11) it is clear that the crown scattering includes N_1 types of scatterers. They are attenuated by the leaves, the stems and the branches. From (7) and (11) we can see that the interaction between the crown constituents appears only in the loss factors and not in the scattering matrix.

2) *The Crown-Ground Interaction*: The bistatic scattering coefficient due to the crown-ground interaction can be written as a sum of two separate terms:

$$\sigma_{pq}(c \leftrightarrow g) = \sigma_{pq}(c \rightarrow g) + \sigma_{pq}(g \rightarrow c). \quad (12)$$

The first term in (12) represents scattering from the crown followed by scattering from the ground while the second term is associated with scattering from the ground followed by scattering from the crown. The explicit contents of these terms are

$$\sigma_{pq}(c \rightarrow g) =$$

$$L_{1p}(\theta_s)L_{2p}(\theta_s) \int_0^{2\pi} d\phi_t \int_0^{\pi/2} \sin \theta_t d\theta_t \sum_{u=v,h} L_{2u}(\theta_t) \cdot \sigma_{pu}^*(\theta_s, \phi_s; \theta_t, \phi_t) Q_{1uq}(\pi - \theta_t, \phi_t; \pi - \theta_i, \phi_i) \cdot \cos \theta_i \left(\frac{L_{1u}(\theta_t) - L_{1q}(\theta_i)}{k_{1q}(\theta_i) \cos \theta_t - k_{1u}(\theta_t) \cos \theta_i} \right) \quad (13a)$$

$$\sigma_{pq}(g \rightarrow c) =$$

$$L_{1q}(\theta_i)L_{2q}(\theta_i) \int_0^{2\pi} d\phi_t \int_0^{\pi/2} \sin \theta_t d\theta_t \sum_{u=v,h} L_{2u}(\theta_t) \cdot Q_{1pu}(\theta_s, \phi_s; \theta_t, \phi_t) \sigma_{uq}^*(\theta_t, \phi_t; \pi - \theta_i, \phi_i) \cdot \cos \theta_s \left(\frac{L_{1p}(\theta_s) - L_{1u}(\theta_t)}{k_{1u}(\theta_t) \cos \theta_s - k_{1p}(\theta_s) \cos \theta_t} \right). \quad (13b)$$

The physical meaning of (13a) can be explained as follows. The quantity $Q_{1uq}(\pi - \theta_t, \phi_t; \pi - \theta_i, \phi_i)$ represents the scattered signal from a unit volume located at z within the crown layer in $(\pi - \theta_t, \phi_t)$ direction. Such a volume scattering generally causes depolarization. The incident wave on a scatterer at z is attenuated by a loss factor equal to $\exp[k_{1q}(\theta_i)z \sec \theta_i]$. For the scattered signal to reach the crown-trunk interface it is attenuated by a loss factor equal to $\exp[-k_{1u}(\theta_t)(z + d_1) \sec \theta_t]$. The integration of these two loss factors over the crown depth gives the quantity in the bracket in (13a). The $L_{2u}(\theta_t)$ is the loss factor associated with the scattered signal passing through the trunk layer to the soil interface. For this signal to be scattered by the ground and to propagate to the receiver through the trunk and the crown layers, it should be modified by $L_{1p}(\theta_s)L_{2p}(\theta_s)\sigma_{pu}^*(\theta_s, \phi_s; \theta_t, \phi_t)$. The integration over $d\theta_t$ and $d\phi_t$ accounts for all possible scattering directions through which the signal is scattered from the canopy and propagates toward the ground. The summation over u in (13a) accounts for the possible polarization combinations. It is clear that in the plane of incidence or for a specular soil surface, there is no cross-polarized scattering from the surface and u takes on only one value. Similar interpretation is applicable to (13b). The backscattering coefficient corresponding to (13) is found by letting $\hat{s} = -\hat{i}$. The integrals in (13) can be evaluated numerically by applying Gaussian quadrature technique [30].

For a slightly rough surface, the coherent field is dominating and it will peak around the specular direction [2]. This allows the following approximation of the surface phase function for the coherent component,

$$\sigma_{qq}^*(\theta_i, \phi_i; \pi - \theta_i, \phi_i) = 4\pi \cos \theta_i R_{qq}(\theta_i) \delta(\cos \theta_t - \cos \theta_i) \cdot \delta(\phi_t - \phi_i) \exp(-4k^2 \sigma^2 \cos^2 \theta_i) \quad (14)$$

where $R_{qq}(\theta_t)$ is the Fresnel reflectivity. In this case the backscattering coefficients due to the crown-soil interaction reduce to

$$\sigma_{pq}(c \rightarrow g) = 4\pi \cos \theta_i L_{1p}(\theta_i) L_{2p}^2(\theta_i) R_{pp}(\theta_i) \exp(-4k^2 \sigma^2 \cos^2 \theta_i) \cdot Q_{1pq}(\pi - \theta_i; \pi + \phi_i; \pi - \theta_i, \phi_i) \left(\frac{L_{1p}(\theta_i) - L_{1q}(\theta_i)}{k_{1q}(\theta_i) - k_{1p}(\theta_i)} \right) \quad (15a)$$

$$\sigma_{pq}(g \rightarrow c) = 4\pi \cos \theta_i L_{1q}(\theta_i) L_{2q}^2(\theta_i) R_{qq}(\theta_i) \exp(-4k^2 \sigma^2 \cos^2 \theta_i) \cdot Q_{1pq}(\theta_i, \pi + \phi_i; \theta_i, \phi_i) \left(\frac{L_{1p}(\theta_i) - L_{1q}(\theta_i)}{k_{1q}(\theta_i) - k_{1p}(\theta_i)} \right). \quad (15b)$$

It is clear that (15a) and (15b) satisfy the reciprocity, $\sigma_{pq}(c \rightarrow g) = \sigma_{qp}(g \rightarrow c)$. Hence, only one expression in (15) is needed. For like polarization the direct substitution of $L_{1p}(\theta_i)$ and $L_{1q}(\theta_i)$ in (15) gives an undetermined value for the backscattering coefficient. To find this value we let

$$\zeta = \left\{ \frac{L_{1p}(\theta_i) - L_{1q}(\theta_i)}{k_{1q}(\theta_i) - k_{1p}(\theta_i)} \right\}. \quad (16)$$

Then, substitution of (6) into (16) yields

$$\zeta = L_{1p}(\theta_i) \left\{ \frac{1 - e^{-(k_{1q}(\theta_i) - k_{1p}(\theta_i)) \cdot H_1 \sec \theta_i}}{k_{1q}(\theta_i) - k_{1p}(\theta_i)} \right\}. \quad (17)$$

By using Taylor expansion for the exponent within the bracket in (17) and keeping the first two terms of the expansion we get

$$\zeta = H_1 \sec \theta_i L_{1p}(\theta_i). \quad (18)$$

From (15) and (18) the like polarized backscattering coefficient for a slightly rough surface due to the crown-ground interaction can be approximated as

$$\sigma_{pp}(g \rightarrow c) = 4\pi H_1 Q_{1pp}(\theta_i, \pi + \phi_i; \theta_i, \phi_i) \cdot R_{pp}(\theta_i) \exp(-4k^2 \sigma^2 \cos^2 \theta_i) \cdot [L_{1p}(\theta_i) L_{2p}(\theta_i)]^2. \quad (19)$$

This above result will also hold for $\sigma_{pp}^o(c \rightarrow g)$ due to reciprocity.

3) Trunk Scattering: The bistatic scattering coefficient of the trunk can be written as (illustrated in the backscattering direction by 3 in Fig. 1);

$$\sigma_{pq}(t) = 4\pi L_{1p}(\theta_s) L_{1q}(\theta_i) Q_{2pq}(\theta_s, \phi_s; \pi - \theta_i, \phi_i) \cdot \left\{ \frac{1 - L_{2p}(\theta_s) L_{2q}(\theta_i)}{k_{2p}(\theta_s) \sec \theta_s + k_{2q}(\theta_i) \sec \theta_i} \right\} \cdot Q_{2pq}(\theta_s, \phi_s; \pi - \theta_i, \phi_i) = \sum_{m=1}^{N_2} n_m (|F_{mpq}(\hat{s}, \hat{i})|^2) \quad (20)$$

where $F_{mpq}(\hat{s}, \hat{i})$ is the element of the scattering amplitude matrix for a scatterer within a trunk group m ($m = 1, \dots, t$). The scattering mechanism in (20) is similar to that in (11) except the scattered signal from the trunk layer is modified by an attenuation factor $[L_{1p}(\theta_s) L_{1q}(\theta_i)]$ due to the crown layer.

4) Trunk-Ground Interaction: Similar to the crown-ground interaction, the trunk-ground interaction consists of two terms (illustrated in the backscattering direction by 5 in Fig. 1)

$$\sigma_{pq}(t \leftrightarrow g) = \sigma_{pq}(t \rightarrow g) + \sigma_{pq}(g \rightarrow t). \quad (21)$$

The first term in (21) represents scattering from the trunk followed by scattering from the ground. The second term represents scattering from the ground followed by scattering from the trunk. The explicit expressions for these two terms are

$$\sigma_{pq}(t \rightarrow g) = L_{1p}(\theta_s) L_{1q}(\theta_i) L_{2p}(\theta_s) \int_0^{2\pi} d\phi_t \int_0^{\pi/2} \sin \theta_t d\theta_t \sum_{u=v,h} \sigma_{pu}^s(\theta_s, \phi_s; \theta_t, \phi_t) \cdot Q_{2uq}(\pi - \theta_t, \phi_t; \pi - \theta_i, \phi_i) \cdot \cos \theta_i \left[\frac{L_{2u}(\theta_t) - L_{2q}(\theta_i)}{k_{2q}(\theta_i) \cos \theta_t - k_{2u}(\theta_t) \cos \theta_i} \right] \quad (22a)$$

$$\sigma_{pq}(g \rightarrow t) = L_{1p}(\theta_s) L_{1q}(\theta_i) L_{2q}(\theta_i) \int_0^{2\pi} d\phi_t \int_0^{\pi/2} \sin \theta_t d\theta_t \sum_{u=v,h} Q_{2pu}(\theta_s, \phi_s; \theta_t, \phi_t) \sigma_{uq}^s(\theta_t, \phi_t; \pi - \theta_i, \phi_i) \cdot \cos \theta_s \left[\frac{L_{2p}(\theta_s) - L_{2u}(\theta_t)}{k_{2u}(\theta_t) \cos \theta_s - k_{2p}(\theta_s) \cos \theta_t} \right]. \quad (22b)$$

The quantity $Q_{2uq}(\theta_s, \phi_s; \theta_t, \phi_t)$ in (22b) is the scattered intensity per unit volume within the trunk layer. The quantity in bracket is the loss factor for volume scattering in the trunk region. Similar interpretation applies to quantities in (22a).

Similar to the crown-ground interaction (13) the integration over θ_t and ϕ_t can be performed by Gaussian quadrature [30]. For a specular or a slightly rough surface and backscattering direction, (22) can be approximated by

$$\sigma_{pq}(t \rightarrow g) = 4\pi \cos \theta_i L_{1p}(\theta_i) \cdot L_{1q}(\theta_i) \cdot R_{pp}(\theta_i) \exp(-4k^2 \sigma^2 \cos^2 \theta_i) \cdot Q_{2pq}(\pi - \theta_i, \pi + \phi_i; \pi - \theta_i, \phi_i) \cdot \left[\frac{L_{2p}(\theta_i) - L_{2q}(\theta_i)}{k_{2q}(\theta_i) - k_{2p}(\theta_i)} \right] \cdot L_{2p}(\theta_i) = \sigma_{qp}(g \rightarrow t). \quad (23)$$

Following the derivation indicated in (16)–(18) we obtain the like polarized coefficients in the backward direction due to trunk-ground interaction as

$$\sigma_{pp}(g \rightarrow t) = 4\pi H_2 Q_{2pp}(\theta_i, \pi + \phi_i; \theta_i, \phi_i) [L_{1p}(\theta_i) \cdot L_{2p}(\theta_i)]^2 \cdot R_{pp}(\theta_i) \exp(-4k^2 \sigma^2 \cos^2 \theta_i). \quad (24)$$

C. The Second-Order Solution The second-order solution of the radiative transfer equation with respect to the crown layer albedo is obtained by using the first-order intensity within the canopy as an exciting source. This solution contains many terms, but most of these terms are small compared to the first-order solution. In this study only two dominant terms are kept. These terms are due to scattering within the crown layer. One significant difference between the first- and second-order terms is that the input to the first-order scattering usually involves only one Stokes parameter while the input to the second-order

scattering consists of all four Stokes parameters. The scattering process associated with each term is illustrated in Fig. 4 and their contribution to the bistatic scattering coefficient is given by

$$\sigma_{pq}^2 = \sigma_{pq}(+, +, -) + \sigma_{pq}(+, -, -) \quad (25)$$

where

$$\begin{aligned} \sigma_{pq}(+, +, -) = & 4\pi \int_0^{\pi/2} \sin \theta_t d\theta_t \int_0^{2\pi} d\phi_t \\ & \cdot \left[\sum_{u=v,h} \frac{\cos \theta_i Q_{1pu}(\theta_s, \phi_s; \theta_t, \phi_t)}{k_{1u}(\theta_t) \cos \theta_i + k_{1q}(\theta_i) \cos \theta_t} \right. \\ & \cdot Q_{1uq}(\theta_t, \phi_t; \pi - \theta_i, \phi_i) \left\{ \frac{1 - L_{1p}(\theta_s) L_{1q}(\theta_i)}{k_{1p}(\theta_s) \sec \theta_s + k_{1q}(\theta_i) \sec \theta_i} \right. \\ & + L_{1q}(\theta_i) \frac{L_{1u}(\theta_t) - L_{1p}(\theta_s)}{k_{1u}(\theta_t) \sec \theta_t - k_{1p}(\theta_s) \sec \theta_s} \left. \right\} \\ & + 2\text{Re} \left(\frac{\cos \theta_i Q_{1p3}(\theta_s, \phi_s; \theta_t, \phi_t)}{k_{13}(\theta_t) \cos \theta_i + k_{1q}(\theta_i) \cos \theta_t} \right. \\ & \cdot Q_{13q}(\theta_t, \phi_t; \pi - \theta_i, \phi_i) \left\{ \frac{1 - L_{1p}(\theta_s) L_{1q}(\theta_i)}{k_{1p}(\theta_s) \sec \theta_s + k_{1q}(\theta_i) \sec \theta_i} \right. \\ & + L_{1q}(\theta_i) \frac{L_{13}(\theta_t) - L_{1p}(\theta_s)}{k_{13}(\theta_t) \sec \theta_t - k_{1p}(\theta_s) \sec \theta_s} \left. \right\} \left. \right] \quad (26a) \end{aligned}$$

$$\begin{aligned} \sigma_{pq}(+, -, -) = & 4\pi \int_0^{\pi/2} \sin \theta_t d\theta_t \int_0^{2\pi} d\phi_t \\ & \cdot \left[\sum_{u=v,h} \frac{\cos \theta_s Q_{1pu}(\theta_s, \phi_s; \pi - \theta_t, \phi_t)}{k_{1u}(\theta_t) \cos \theta_s + k_{1p}(\theta_s) \cos \theta_t} \right. \\ & \cdot Q_{1uq}(\pi - \theta_t, \phi_t; \pi - \theta_i, \phi_i) \left\{ \frac{1 - L_{1p}(\theta_s) L_{1q}(\theta_i)}{k_{1p}(\theta_s) \sec \theta_s + k_{1q}(\theta_i) \sec \theta_i} \right. \\ & + L_{1p}(\theta_s) \frac{L_{1u}(\theta_t) - L_{1q}(\theta_i)}{k_{1u}(\theta_t) \sec \theta_t - k_{1q}(\theta_i) \sec \theta_i} \left. \right\} \\ & + 2\text{Re} \left(\frac{\cos \theta_s Q_{1p3}(\theta_s, \phi_s; \pi - \theta_t, \phi_t)}{k_{13}(\theta_t) \cos \theta_s + k_{1p}(\theta_s) \cos \theta_t} \right. \\ & \cdot Q_{13q}(\pi - \theta_t, \phi_t; \pi - \theta_i, \phi_i) \left\{ \frac{1 - L_{1p}(\theta_s) L_{1q}(\theta_i)}{k_{1p}(\theta_s) \sec \theta_s + k_{1q}(\theta_i) \sec \theta_i} \right. \\ & + L_{1p}(\theta_s) \frac{L_{13}(\theta_t) - L_{1q}(\theta_i)}{k_{13}(\theta_t) \sec \theta_t - k_{1q}(\theta_i) \sec \theta_i} \left. \right\} \left. \right] \quad (26b) \end{aligned}$$

where $\text{Re}(\cdot)$ is the real part operator and,

$$\begin{aligned} Q_{1v3}(\theta_s, \phi_s; \theta_t, \phi_t) &= \sum_{m=1}^{N_1} n_m \langle F_{mvv}(\hat{s}, \hat{i}) F_{mvh}^*(\hat{s}, \hat{t}) \rangle \\ Q_{13v}(\theta_s, \phi_s; \theta_t, \phi_t) &= \sum_{m=1}^{N_1} n_m \langle F_{mvv}(\hat{s}, \hat{i}) F_{mhh}^*(\hat{s}, \hat{t}) \rangle \\ Q_{13h}(\theta_s, \phi_s; \theta_t, \phi_t) &= \sum_{m=1}^{N_1} n_m \langle F_{mvh}(\hat{s}, \hat{i}) F_{mhh}^*(\hat{s}, \hat{t}) \rangle \\ Q_{1h3}(\theta_s, \phi_s; \theta_t, \phi_t) &= \sum_{m=1}^{N_1} n_m \langle F_{mhv}(\hat{s}, \hat{i}) F_{mhh}^*(\hat{s}, \hat{t}) \rangle \quad (27) \end{aligned}$$

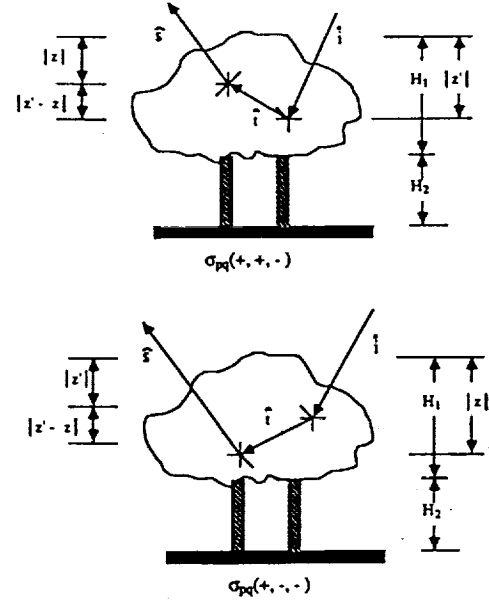


Fig. 4. The scattering processes in (26) associated with the second-order solution of the radiative transfer equation.

with $*$ is the complex conjugate operator. In addition

$$\begin{aligned} k_{13}(\theta_t) &= \frac{1}{2} [k_{1v}(\theta_t) + k_{1h}(\theta_t)] \\ &+ \frac{2\pi j}{k} \text{Re} \left[\sum_{m=1}^{N_1} n_m \langle F_{mvv}(\hat{i}, \hat{t}) - F_{mhh}(\hat{i}, \hat{t}) \rangle \right] \\ L_{13}(\theta_t) &= \exp[-k_{13}(\theta_t) H_1 \sec \theta_t]. \quad (28) \end{aligned}$$

The processes of scattering in (26a) are illustrated in Fig. 4. From this figure we see that $\sigma_{pq}(+, +, -)$ represents scattering by a unit volume first from direction $\hat{i}(\pi - \theta_i, \phi_i)$ to direction $\hat{i}(\theta_t, \phi_t)$ and then by another unit volume from direction $\hat{i}(\theta_t, \phi_t)$ to the observation direction $\hat{s}(\theta_s, \phi_s)$. These two processes are represented by the quantities $Q_{1pu}(\theta_s, \phi_s; \theta_t, \phi_t)$ $Q_{1uq}(\theta_t, \phi_t; \pi - \theta_i, \phi_i)$ for the first two Stokes parameters and by $Q_{1p3}(\theta_s, \phi_s; \theta_t, \phi_t)$ $Q_{13q}(\theta_t, \phi_t; \pi - \theta_i, \phi_i)$ for the last two Stokes parameters. To reach the first scattering volume the incident wave is attenuated by $e^{k_{1q}(\theta_i) z' \sec \theta_i}$. In going from the first to the second scattering volume, the wave is further attenuated by $e^{k_{1u}(\theta_i)(z' - z) \sec \theta_i}$. After the second scattering the scattered wave with p polarization is attenuated by $e^{k_{1p}(\theta_s) z \sec \theta_s}$ before it reaches the canopy-air interface. The integration of the product of these loss factors over dz' and dz ($-H_1 \leq z' \leq z$, and $-H_1 \leq z \leq 0$) gives the other quantities in (26a). The summation in (26a) accounts for the first and second Stokes' parameters of the scattered wave in $\hat{i}(\theta_t, \phi_t)$ direction. The $\text{Re}(\cdot)$ comes from summing the last two Stokes' parameters $\hat{i}(\theta_t, \phi_t)$. The integration over $d\theta_t$ and $d\phi_t$ accounts for all possible scattering directions through which the signal scattered from location z' toward location z . Similar interpretation is applicable to $\sigma_{pq}(+, -, -)$ in (26b).

From (26)–(28) it is clear that the second-order solution requires all the four Stokes parameters. Also we can see that

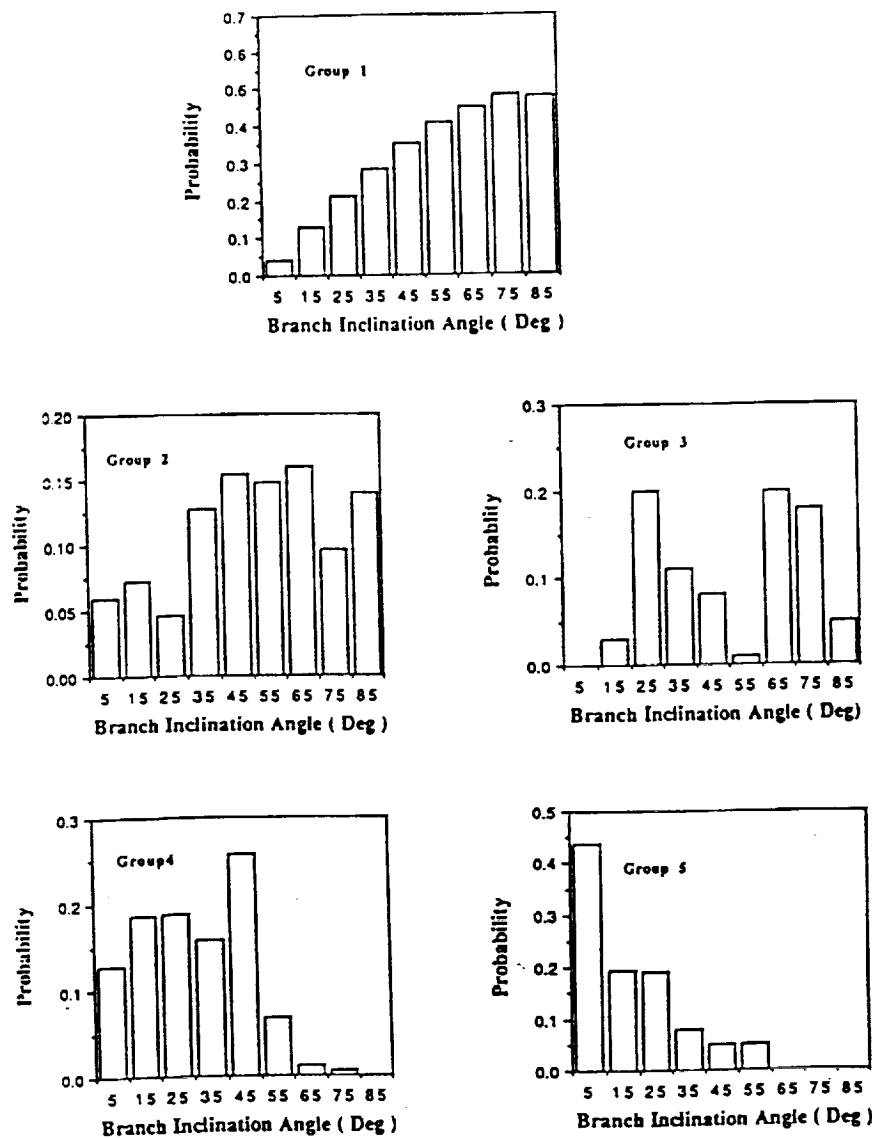


Fig. 5. The probability distributions of the inclination angles for different groups of branches.

TABLE I
THE PARAMETER FOR EACH BRANCH GROUP

Branch Group	Diameter Range (cm)	Average Diameter (cm)	Average Length (cm)	Number density (m^{-3})
1 /stems	0.0–0.40	0.10	18	250
2	0.5–1.90	1.28	14	11.4
3	2.0–2.90	2.60	32	0.43
4	3.0–6.90	5.00	58	0.33
5 /trunk	7.0–17.1	9.00	76	0.14

the second-order solution includes scattering due to interaction between the forest components.

IV. GROUND TRUTH DATA, NUMERICAL RESULTS AND ANALYSIS

In this section comparisons of this model with backscattering measurements from both deciduous and coniferous forest, are carried out to verify the model validity. In addition, the

effects of frequency, second-order interaction, and surface roughness as it impacts tree-ground interaction are illustrated to indicate the model major advantages. Results are organized into three subsections. In the first subsection, the characteristics of a deciduous and a coniferous canopy and the associated ground truth are described. The second subsection shows comparisons between the calculated and measured values of the backscattering coefficients for walnut canopy at L and X bands and for cypress trees at S and X bands. Furthermore, illustrations are given showing the contribution of each canopy component to the total backscattering coefficient. The third subsection presents some numerical results to indicate how frequency, second-order interaction, and surface roughness affect the backscattering coefficients.

A. Deciduous and Coniferous Canopy Characteristics

In this study the walnut canopy and the cypress trees are taken to represent a deciduous and a coniferous canopy respectively. We shall begin by describing the walnut canopy

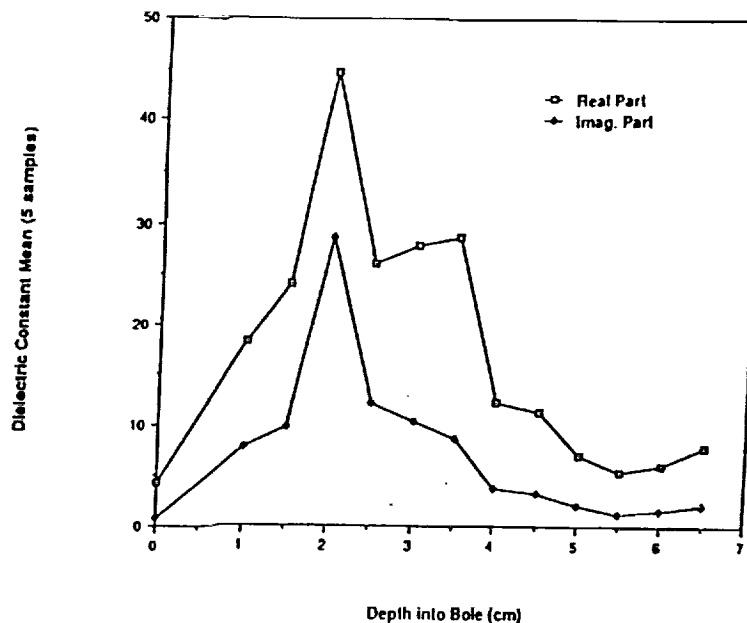


Fig. 6. The relative dielectric constant as a function of depth into walnut bole.

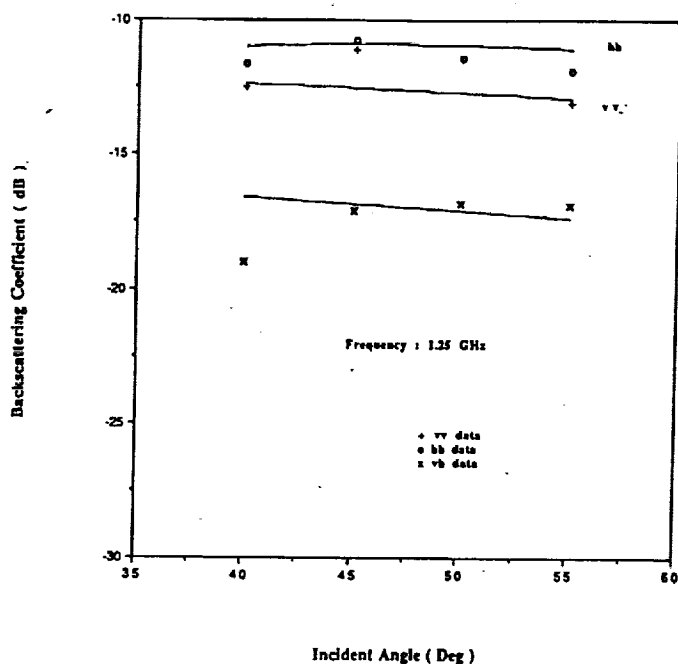


Fig. 7. Comparisons of theoretical and experimental backscattering coefficients for a walnut canopy at L band as a function of the incident angle.

TABLE II
DIELECTRIC CONSTANT VALUES

Frequency Band	L	X
Leaves	$19.58-j\ 5.54$	$14.9-j\ 4.9$
branch/stems	$27.3-j\ 8.4$	$20.0-j\ 9.7$
soil	$5.00-j\ 0.7$	$5.00-j\ 0.7$

and its parameters and then the cypress trees.

1) The Walnut Canopy Characteristics:

The canopy consists of 6-year-old black walnut trees [26, Sec. V, Vol I]. The trees have an average height of 4.8 m.

Their geometry data was collected in two parts. Measurements involving branches with diameter greater than 4 cm were termed skeleton geometry measurements and the rest higher order measurements. A group of 16 walnut trees was chosen for the canopy geometry and ground truth measurements. Their heights, width across the row, and the length down the row were measured. The skeleton branches which terminated into a successively smaller diameter branch were physically sampled for their length, diameter, and inclination angle for all 16 trees. Small branches that grew along the skeleton tend to fill the interior of the canopy. Such branches with diameter less than 4 cm were sampled only for a couple of trees. The thinnest branches with diameter less than 1 cm and length less than 30 cm, were not sampled for their inclination orientations. The branches were grouped into four different groups according to their radius, and for each group an average length of the branch was computed. Beside these four branch groups, there are green stems which have an external covering of green bark and are located just below the juncture with the petioles. For modeling purposes we will consider the stems as a group of branches. The stem group will be labeled as group #1 among the other branch groups. Table I sums up the relevant parameters for each branch group type.

From the inclination angle measurements of the branches, the inclination angle probabilities for all branch groups are calculated. Fig. 5 presents the histograms of the inclination angle probabilities for different radius groups. The data show that as the diameter of the branch increases, it tends to become vertical. The thin branches do not show any preferred inclination.

The leaves were found to be growing only on the branches in groups 1 and 2. The leaves on group 2 branches were determined from the routine sampling of higher order canopy geometry measurements. However, due to the large number of branches in group 1, an exclusive sampling was done to

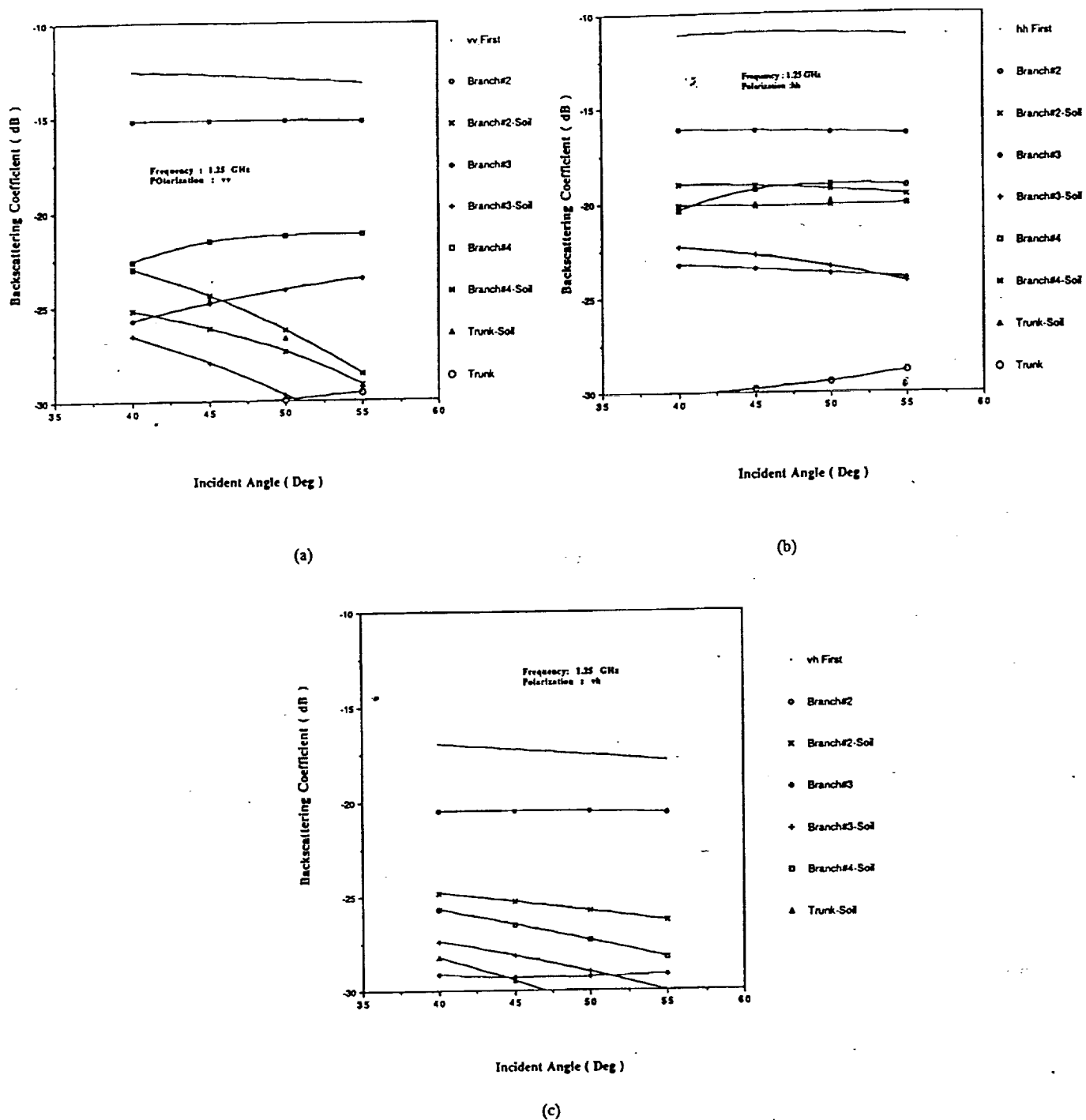


Fig. 8. Illustrations of the contributions by the walnut canopy components in first-order backscattering for (a) VV, (b) HH, and (c) VH polarizations at L band.

estimate the number of leaves per branch in the group 1 category. This leaf data was extrapolated to cover the whole canopy. The average density of the leaves was 250 m^{-3} [15]. Each leaf had an average leaf area of 254 square cm and on the average there were five leaflets on one leaf. Assuming the leaves to be circular, the leaf area results gave the average disc radius of approximately 3.6 cm and a thickness equal to 0.1 mm. The leaf inclination angle has a probability distribution function equal to $\sin \beta (0^\circ < \beta < 90^\circ)$.

In situ measurements of dielectric constant of stems, branches, and leaves were made by a team from the University of Michigan at L band ($f = 1.2 \text{ GHz}$). An electric probe

was inserted into a hole drilled into a branch to find the dielectric constant [26, Sec. XIII, Vol. II]. The leaves were stacked in layers upon a flat piece of wood. For each stack, the probe reading was noted at three separate locations on the stack. The behavior of the dielectric constant with depth inside a branch or on a stack of leaves was found from probe readings. Fig. 6 shows the relative dielectric constant as a function of depth into walnut bole. It is clear the dielectric constant real part has values between 4 and 45. The imaginary part varies between 1 and 30. For stem dielectric constant a representative value at the L band is found to be $27.3 - j 8.4$. As this value for the dielectric constant is a mean value for

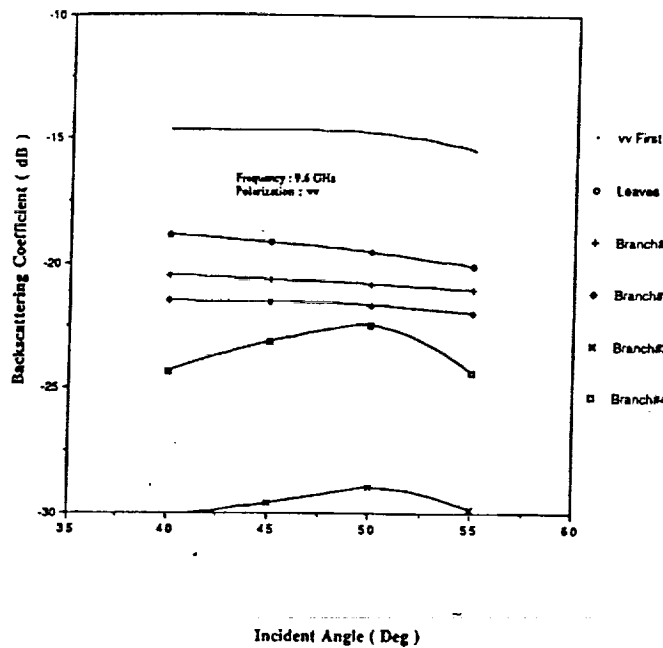


Fig. 9. Comparisons of theoretical and experimental backscattering coefficients for a walnut canopy at X band as a function of the incident angle.

TABLE III
GROUND TRUTH FOR CYPRESS TREE SCATTERER

	Leaves	Branch#1	Branch#2	Branch#3
Length (cm)	1	13	18	20
Radius (cm)	0.1	0.12	0.3	1
Number	0.796×10^5	400	64	10
Density (m^{-3})				
B_m (°)	90	90	90	0.0
B_0 (°)	0.0	0.0	0.0	10
B_1 (°)	0.0	0.0	0.0	0.0
B_2 (°)	90	90	90	60
n	2	1	1	6

the bole dielectric constant, it will be taken as representative value for branch dielectric constant. The leaf dielectric value varies from $8.77 - j 2.88$ to $19.58 - j 5.54$ according to the number of the leaves stacked in layers upon a flat piece of wood to measure the dielectric constant. Consequently, an average value $19.58 - j 5.54$ will be used to represent the leaf dielectric constant. There is no independent confirmation of the leaf and branch dielectric constant values as high as used in [14].

The soil relative dielectric constant measurements were repeated on hourly basis. Each observation sequence consisted of three types of data designated: wet, dry, and mix. The wet and dry consisted of separate samples of the soil surface regions which were always wet or always dry, respectively. A transect sampling was used to evaluate the spatial average of the dielectric constant over the three moisture regions. The dielectric transect data consisted of 22 samples spaced 0.3 m apart and extending from center of one row to the center of the next. The location of the transect along a row with respect to the tree and sprinkler location was randomized. The sprinklers were placed along the rows of the trees to irrigate the trees. The water from sprinklers was sprayed in an approximately 3-ft wide strip along the rows of the trees. There was no

sprinkler in between the tree rows. Thus approximately 70% of the area was not irrigated and thus can be classified as "dry soil." It was found that inter-row dielectric constant has values between $18.48 - j 1.6$ and $2.79 - j 0.16$. Furthermore, ten soil samples taken from area partially covered by organic leaf litter showed an average dielectric constant value of $2.96 - j 0.49$. In addition, the spatial averaging for backscatter as seen by the radar was done by rotating the boom across the rows in an arc and it was not done along the tree rows. Accordingly, we believe that the ground dielectric constant should have a small average value which is taken to be $5.0 - j 0.7$.

To obtain the values of the leaf and branch dielectric constant at X band ($f = 9.6$ GHz), the corresponding values at L band are incorporated in Ulaby and El Rayes' dielectric constant formula [31] to obtain the leaf and branch gravimetric moisture contents (0.55 for leaves and 0.65 for branches). By substituting these values for the moisture contents along with the X band frequency into Ulaby and El Rayes formula, we obtain the values of the dielectric constant at X band ($14.9 - j 4.9$ for leaves and $20. - j 9.7$ for branches). Since the soil effect at X band is unimportant in the backscattering calculation, its dielectric constant is not estimated at X band. Table II sums up the dielectric constant values used for the leaves and stems and branches.

For the purpose of modeling we divide the canopy into two layers above a rough interface. The upper layer with a depth of 3 m is the crown layer and the lower layer with a depth of 1.7 m is for the trunk layer. The crown layer contains leaves and the first four branch groups. The fifth branch group is included in the trunk layer. The soil-canopy interface roughness is represented by a Gaussian correlation function with σ and L given by 0.021 m and 0.25 m, respectively. In calculating the crown- and trunk-soil interaction terms (13), (22) the soil scattering coefficient $\sigma_{pu}^s(\theta_s, \phi_s; \theta_t, \phi_t)$ is obtained by summing up the coherent (Eq. 12.52 of [2]) and the noncoherent (Eq. 12.55 of [2]) scattering terms.

2) *The Cypress Tree Characteristics:* The cypress trees with the same height and nearly the same density are considered [4]. They are 3-4 years old. Their trunks are thin, having a diameter of 1-2 cm. The average height of the canopy was about 70 cm. The canopy without leaves is composed of a large number of randomly oriented thin branches and a small number of thin vertical trunks. The leaflets of cypress form a thin rod shape, with length of 1 cm and a diameter of 2 mm, and the whole assembly comprises a relatively flat planar structure. The ground plane is covered with microwave absorbers so that canopy ground interaction effect is unimportant. In this study a one layer model (crown) is used since the trunk height is small. The canopy constituents are grouped into four groups, one group for the leaves; three other groups for the branches. The scatterer inclination angle distribution (β) is governed by the following probability distribution function

$$P(\beta) = A \cos^n \left[\frac{\pi}{2} \left(\frac{\beta - \beta_m}{\beta_0 - \beta_m} \right) \right] \quad \beta_1 \leq \beta \leq \beta_2$$

$$= 0 \quad \text{otherwise} \quad (29)$$

where A is the normalization factor, and n is the shape factor. The probability density function $P(\beta)$ has its maximum value at β_m , and is equal to zero at β equal to β_0 . By adjusting the values of $\beta_0, \beta_1, \beta_2, \beta_m$, and n , the probability density function $P(\beta)$ in (29) can include a variety of probability density functions reported in the literature [32].

The dielectric constants of the coniferous scatterers (needle leaves, and branches) are obtained by employing Ulaby and El-Rayes' formula [31] which gives the dielectric constant in terms of the gravimetric moisture content. For cypress trees under consideration, the reported values for the leaf and branch gravimetric moisture contents are around 58.

B. Comparisons with Backscatter Measurements from Walnut Orchard Canopy

Several sets of microwave data were collected from the walnut canopy [26]. In this study we shall consider two sets of multi-angle data in which the same set of trees were observed at incident angles ranging from 40° to 55° at two different frequencies, 1.25 GHz (L band) and 9.6 GHz (X band). The data were collected over a time span of about 2 hours during mid-afternoon, so the variation in the dielectric constant due to the change of environment can be neglected. The model was evaluated as a function of look angle for frequencies 1.25 and 9.6 GHz using the ground truth reported in Tables I and II and Fig. 5. The model output is given in Figs. 7–10. Figs. 7 and 9 show comparisons of measured and calculated scattering coefficients for three different polarizations at L band and X band, respectively. Figs. 8 and 10 show the contributions of the individual tree components to the total backscattering coefficients, excluding those more than 15 dB below the total.

At L band (Fig. 7) there is a good agreement between theory and measurements. The like polarized backscattering coefficients σ_{vv} and σ_{hh} have the same angular trends with $\sigma_{vv} < \sigma_{hh}$. The cross polarization σ_{vh} is below the like by about 6 dB. Fig. 8 indicates that the main contribution to the like and cross backscattering coefficients is due to branch group #2. The branches within this group have no preferred orientation and their dimensions are such that their contributions to σ_{vv} and σ_{hh} are approximately the same. Other canopy constituents may be small compared to the wavelength (leaves and branch group #1), or comparable to the wavelength and they are nearly vertically oriented (branch #4 and branch #5). For the small scatterers, their contribution to the like and cross polarization is lower than the noise level. The larger scatterers have radiation pattern with maximum field values confined to the forward direction. Consequently, the scattered field is propagating toward the canopy floor, leading to the soil–canopy interaction terms. Since within the angular range considered in this section, the soil reflectivity is higher for horizontally incident wave than for vertically incident wave, the contribution of the interaction terms are higher for σ_{hh} than σ_{vv} . This is the reason, why $\sigma_{hh} > \sigma_{vv}$. Unlike reference [14] we assume the surface to be moderately wet instead of very wet so that this interaction term is not of major importance in σ_{hh} . We made this choice because the surface truth reported in [26] indicates that the very wet condition is a special situation. Also, the σ_{vv} and σ_{hh} returns

are very close to each other. This can be explained if scattering for σ_{vv} and σ_{hh} is dominated by the same branch group as we have found. However, if σ_{vv} is dominated by one branch group and σ_{hh} is dominated by trunk–ground interaction as indicated in [14], then similar level for σ_{vv} and σ_{hh} must be a coincidence.

At X band, the levels of the backscattering coefficients and the relative levels between polarization components are in agreement with measurements (Fig. 9). An earlier publication [15] did not obtain an agreement at this frequency for cross polarization even though model parameters were readjusted between L band and X band. We believe this is due to several factors: (1) enough groups of branches, i.e., an adequate representation of branch size distribution, (2) second-order effects, and (3) validity of model over a wide enough range of frequencies. At X band the polarized backscattering coefficients have similar angular trends. The cross polarized backscattering coefficient level is below the like polarization by nearly 8 dB. Illustrations of the individual contributors are given in Fig. 10. Here, for like-polarized scattering the leaves and the branch groups #1 and #2 are the most important contributors. At X band, the dimensions of those scatterers (leaves, branch #1, branch #2) are sensitive to the incident wavelength, and they have no preferred orientation. At this frequency, the interactions with the ground surface are negligible. For cross polarized scattering the major contribution comes from branch group #1 which is the smallest branch group (stems). The cause of depolarization appears to be the small cylindrically shaped stem and its orientation distribution. The leaf area is large at X band and hence its depolarization is weak. The $\sin \beta$ function for the leaf orientation distribution also leads to a very small contribution to cross polarization [16], [17], [29].

Comparisons with Backscattering Measurements from Cypress Trees: The measurements from a cypress canopy with and without leaves were reported by Hirose *et al.* [4] at S , C , and X bands for incident angles between 10° and 40° . In this study the S and X band data are selected for comparison. The ground truth given in Table III are used in the model to calculate the backscattering coefficients. Figs. 11(a) and (b) show the comparisons with S band measurements with and without leaves. Results indicate that negligible change takes place due to the presence or absence of leaves at this frequency. The agreement between model and measurements is very good for like and cross polarizations except at 10° incidence in like polarization in Fig. 11(b). This may be due to scattering from the ground which is not well covered with microwave absorber. Similar comparisons at X band are shown in Figs. 12(a) and (b). Here again the agreement between model and measurements is very good. The presence of leaves leads to a 4-dB and a 2-dB increase in like and cross-polarized scattering, respectively. Thus, leaves are important scatterers at X band for cypress as well as the walnut trees discussed in the previous section.

C. Surface Roughness, Frequency and Second-Order Effects

In this section we want to illustrate the effects of soil surface roughness, frequency, and the second-order terms in backscattering.

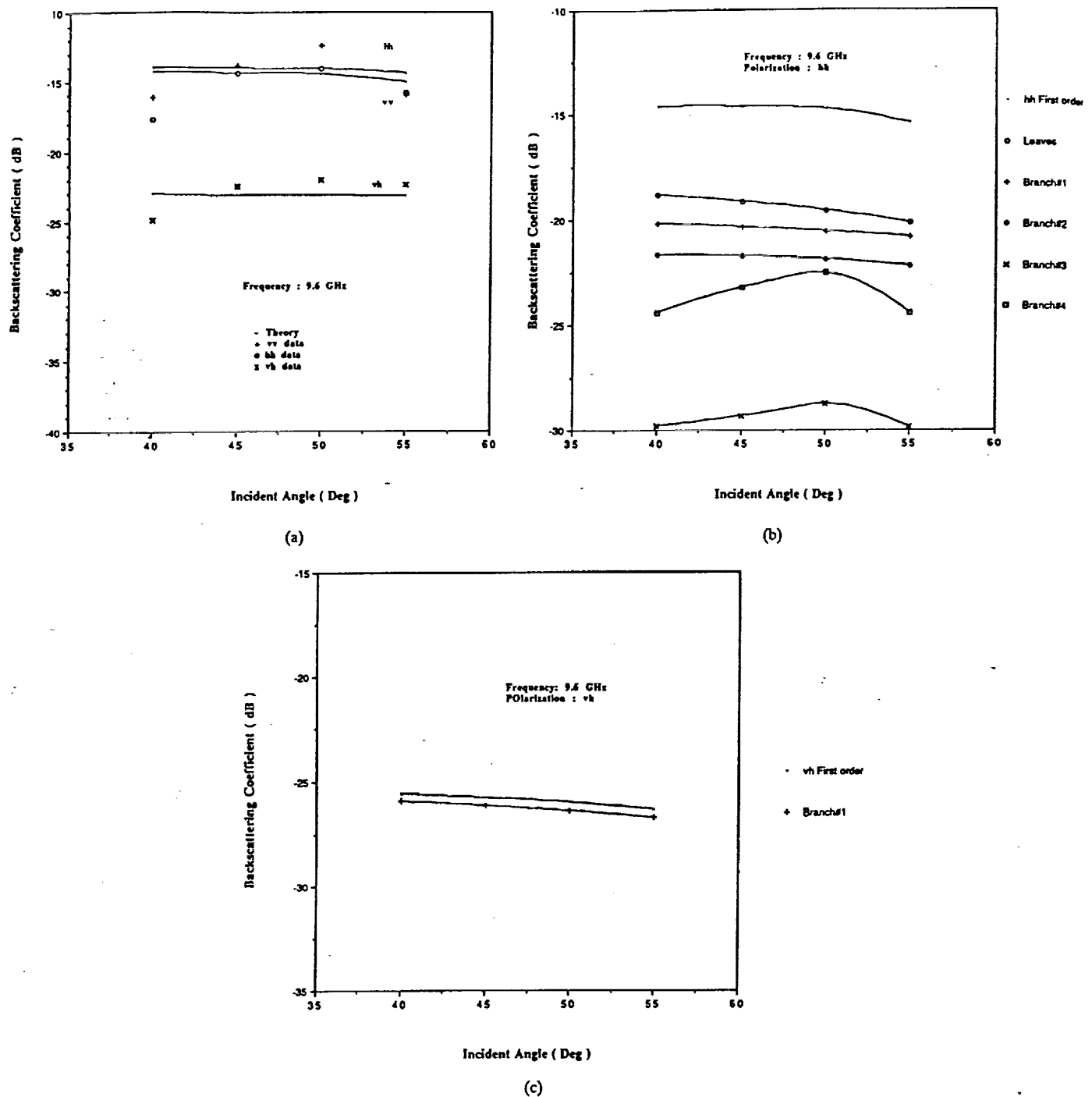


Fig. 10. Illustrations of the contributions by the walnut canopy components in first-order backscattering for (a) VV, (b) HH, and (c) VH polarizations at X band.

1) The Role of Surface Roughness on the Interaction Terms: Scattering due to a rough surface is well known and can be computed easily. Less obvious is how canopy interacts with a plane versus a rough ground surface. More specifically the inclusion of the ground-canopy interaction term is not fully accounted for in the available models [10]–[13] because only a flat ground is considered. To see the difference between the use of a flat versus a rough ground surface we show in Figs. 13(a)–(c) the surface roughness effects on the soil-canopy interaction terms for like and cross polarizations. These figures are generated by using the ground truth reported for walnut

canopy in Tables I and II at L band. For the rough surface the correlation function is taken to be Gaussian and the scattering matrix is obtained by employing the Kirchhoff model along with the scalar approximation [2, Chapter 12].

From these figures we see that the inclusion of surface roughness leads to a reduction in the interaction terms for like polarizations (VV, HH) near nadir incidence but an increase in the like and cross polarization terms at higher incidence angles. The angular range within which the interaction terms are higher for the rough than the plane surface varies from one polarization to another and is expected to vary also with

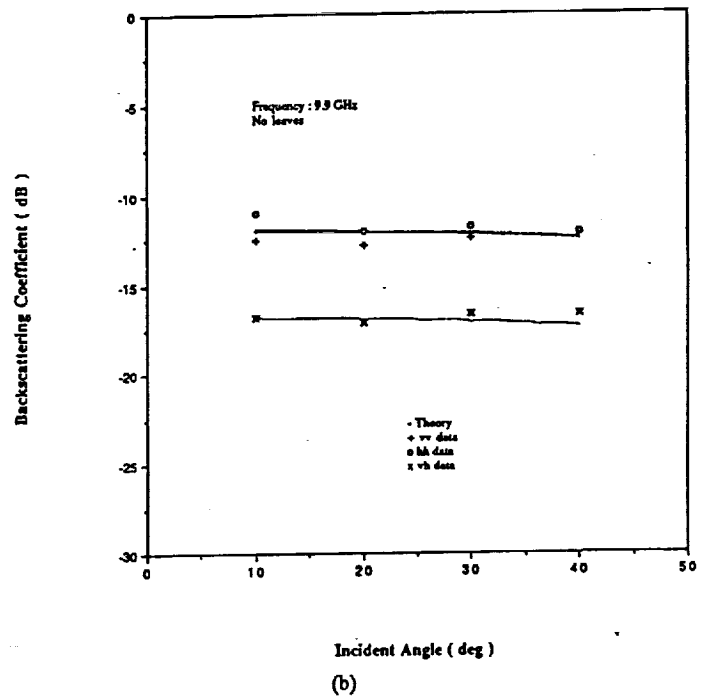
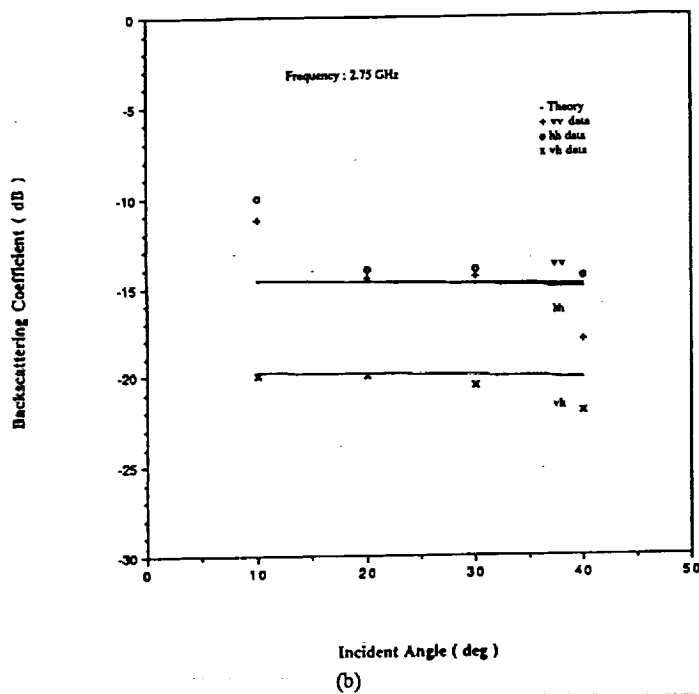
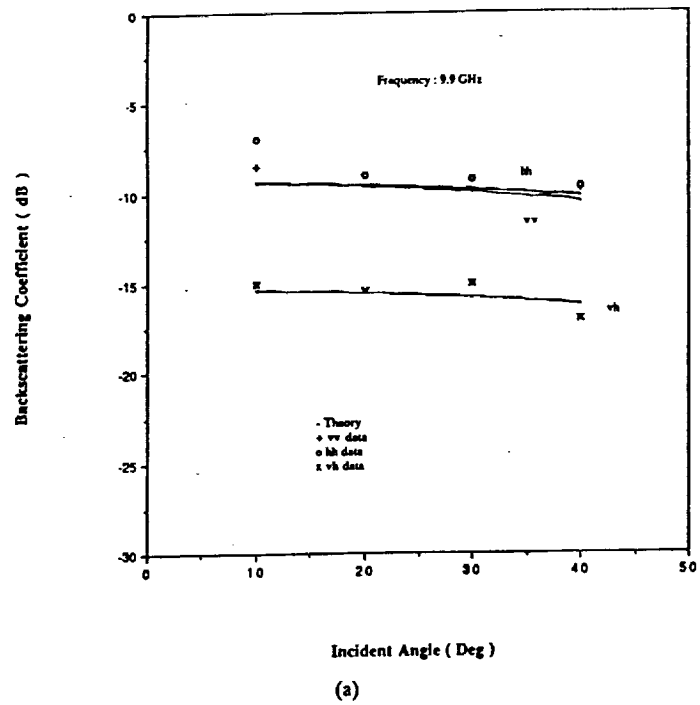
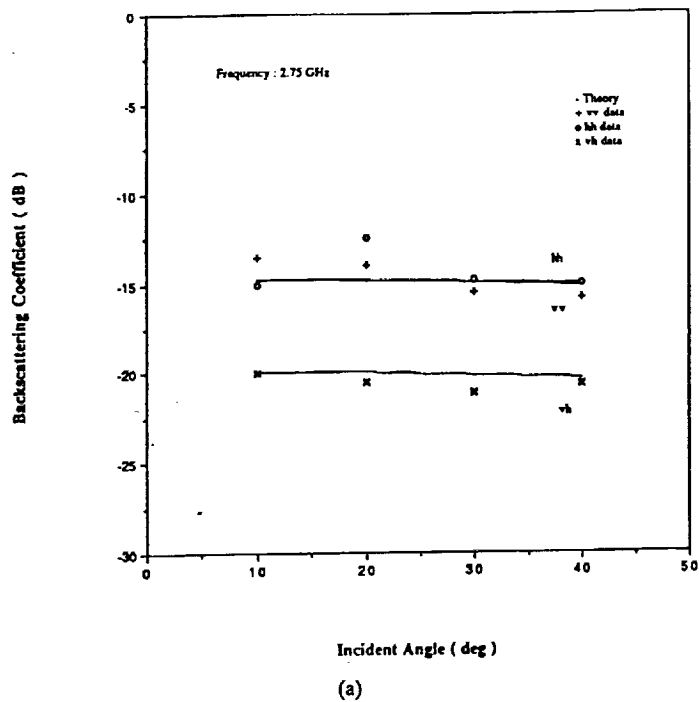


Fig. 11. Comparisons of theoretical and experimental backscattering coefficients for a cypress canopy at *S* band as a function of the incident angle: (a) With leaves. (b) Without leaves.

Fig. 12. Comparisons of theoretical and experimental backscattering coefficients for a cypress canopy at *X* band as a function of the incident angle. (a) With leaves. (b) Without leaves.

a change in the roughness property. While soil roughness is found to be unimportant in the comparisons shown in Section IV.B.1, it is expected to be important when the soil surface is wet.

2) *Second-Order Terms in the Backscattering Coefficients:* The effect of the second-order scattering terms due to branches was not considered in the previous models [11]–[15]. The introduction of the second-order terms in this study is a way to account for the multiple scattering effects within a forested canopy. From the numerical calculations we found that the

second-order terms had little effect on the level and trend of the like polarized signals. Hence, illustrations are limited to cross polarized calculations.

Fig. 14 presents the angular variation of the first- and second-order cross polarized signals (σ_{vh}) at *L* and *X* bands using model parameters for the walnut orchard. It is seen that the second-order term is not important at *L* band but is significant at *X* band. Fig. 15 shows the variation of the cross polarized signal from cypress trees as a function of frequency at 40° angle of incidence. From these figures we see that

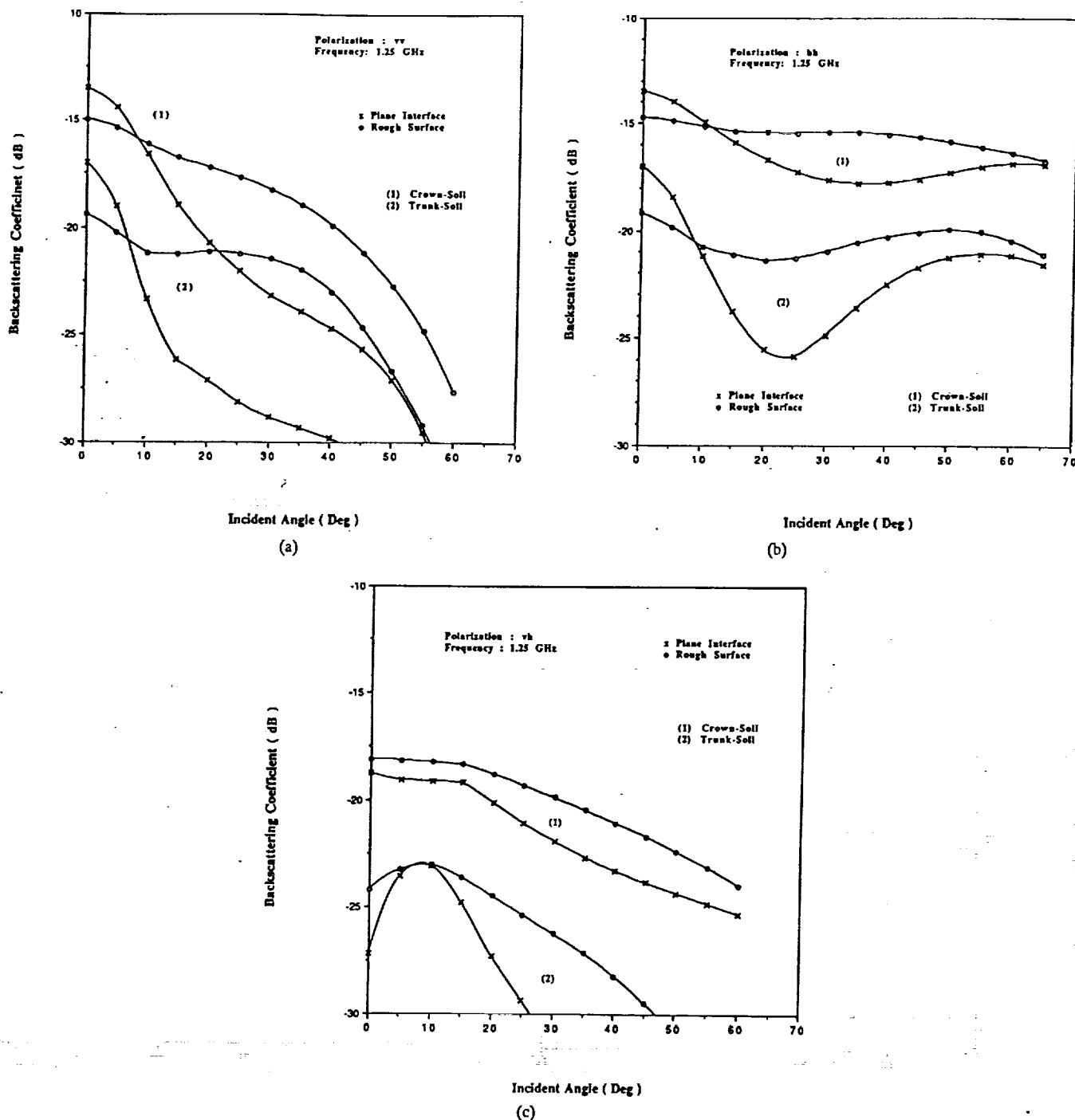


Fig. 13. The effect of including the surface roughness in the canopy-ground interaction on backscattering from a walnut canopy at L band: (a) VV polarization; (b) HH polarization; (c) VH polarization.

the importance of multiple scattering effects are dependent on frequency and canopy parameters.

3) *Frequency Dependence*: One merit of the current model is that it can be applied over a wide frequency band without changing the forest component modeling or adjusting the forest component phase matrices and extinction cross sections. Fig. 16 shows the variation of the backscattering coefficient for cypress trees as a function of the incident frequency at 40° incidence. From this figure we see that for frequency lower than 4 GHz, the backscattering coefficients increase rather quickly with frequency. This increase indicates a Rayleigh

region for the canopy. In the frequency range, 4–8 GHz, the rate of increase of the backscattering coefficients with frequency is much smaller. This corresponds to the resonance region where significant phase interference takes place. For frequencies higher than 8 GHz, the backscattering coefficients have a higher rate of increase with the frequency. This is not necessary true in general but is due to the specific canopy constituents as illustrated in Fig. 17. Here, the needle-shaped leaves happen to have a dimension that is still in the Rayleigh region and hence its contribution increases fast with frequency. In conclusion, the final frequency behavior of a forest canopy

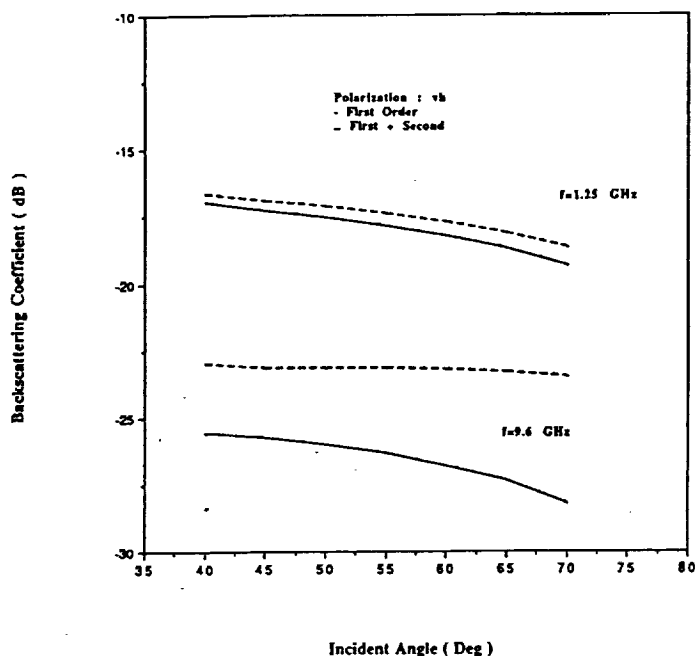


Fig. 14. The angular variation of cross-polarized coefficient for walnut canopy calculated by using the first and second-order solution of the radiative transfer equation at L and X band (parameters of Figs. 7 and 9).

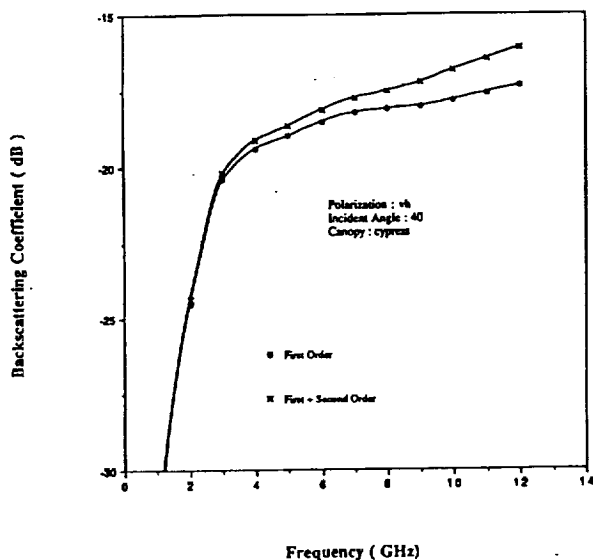


Fig. 15. The variation of the cross-polarized coefficients for cypress trees with the frequency, calculated by using the first and second-order solution of the radiative transfer equation at 40° angle of incidence (parameters as in Figs. 11 and 12).

is dependent on the specific sizes of its components. Hence, it is important to model each canopy component over a wide range of frequency.

V. DISCUSSION

In this paper a microwave scattering model has been developed for layered vegetation and compared with experimental data from walnut and cypress trees. The major advantages of this model are that, it (1) accounts for first- and second-order scattering within the canopy, (2) fully accounts for the surface

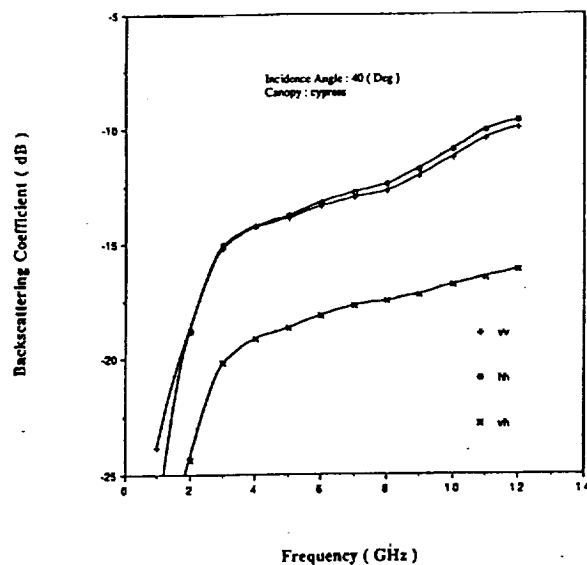


Fig. 16. The variation of the like and cross backscattering coefficients for cypress trees as a function of the incident frequency (parameters as in Figs. 11 and 12).

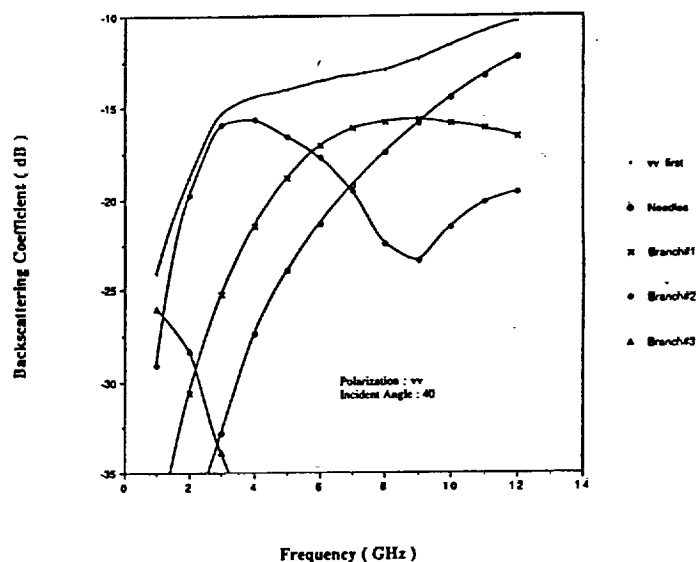


Fig. 17. The components of σ_{vv} for cypress trees as a function of the incident frequency (parameters as in Figs. 11 and 12).

roughness in the canopy-soil interaction terms (3) allows many branch sizes and their orientation distributions and (4) is valid over a wide frequency range for both deciduous and coniferous vegetation.

The application of this model to walnut and cypress trees leads to the following conclusions:

1. To obtain a match between the calculated and measured values of the backscattering coefficients, the branch size distribution is important. In this paper, the branch size distribution has been discretized into four sizes. We expect that the use of only one or two average branch sizes will not be able to explain multifrequency data. This indicates that the structure of a forest is important.
2. Small branches and leaves generally contribute to the backscattering coefficients at X band. In particular, cross

polarization at X band is dominated by stems and not leaves in deciduous trees.

3. The contribution of the trunk-soil interaction to the backscattering coefficients depends heavily on soil moisture and soil roughness and it is more important for σ_{hh} than σ_{vv} polarization.

VI. APPENDIX A

THE ITERATIVE SOLUTION OF THE RADIATIVE TRANSFER EQUATIONS

IN this appendix the radiative transfer equations governing the intensity (Stokes' parameters) within the canopy is presented and the procedures for obtaining their iterative solution is outlined. For simplicity only the radiative transfer equation within the crown layer is considered.

The radiative transfer equations describing the Stokes parameters within the crown layer are [34]:

$$\begin{aligned} \cos \theta \frac{dI(\theta, \phi, z)}{dz} &= -\bar{K}(\theta) \bar{I}(\theta, \phi, z) + \bar{S}(\theta, \phi, z) \\ -\cos \theta \frac{dI(\pi - \theta, \phi, z)}{dz} &= -\bar{K}(\pi - \theta) \bar{I}(\pi - \theta, \phi, z) \\ &\quad + \bar{S}(\pi - \theta, \phi, z) \end{aligned} \quad (A1)$$

where $\bar{I}(\theta, \phi, z)$ and $\bar{I}(\pi - \theta, \phi, z)$ are the upward and downward Stokes parameters at location z with

$$\bar{I}(\theta, \phi, z) = \begin{bmatrix} I_v(\theta, \phi, z) \\ I_h(\theta, \phi, z) \\ I_3(\theta, \phi, z) \\ I_4(\theta, \phi, z) \end{bmatrix} = \begin{bmatrix} \langle |E_v|^2 \rangle \\ \langle |E_h|^2 \rangle \\ 2\text{Re}\langle E_v E_h^* \rangle \\ 2\text{Im}\langle E_v E_h^* \rangle \end{bmatrix}. \quad (A2)$$

E_v and E_h are the vertically and horizontally polarized components for the electric field vectors. In (A1) $\bar{S}(\theta, \phi)$ and $\bar{S}(\pi - \theta, \phi)$ are the upward and downward source functions defined as

$$\begin{aligned} \bar{S}(\theta, \phi, z) &= \int_0^{2\pi} d\phi_t \int_0^{\pi/2} \sin \theta_t d\theta_t \\ &\quad \cdot \sum_{m=1}^{N_1} n_m [\langle \bar{P}_m(\theta, \phi; \theta_t, \phi_t) \rangle \bar{I}(\theta_t, \phi_t, z) \\ &\quad + \langle \bar{P}_m(\theta, \phi; \pi - \theta_t, \phi_t) \rangle \bar{I}(\pi - \theta_t, \phi_t, z)]. \end{aligned} \quad (A3)$$

In (A3) $\bar{P}_m(\theta, \phi; \theta_t, \phi_t)$ is a 4×4 phase matrix of the m th group of scatterers. This matrix describes the scattering properties from direction (θ_t, ϕ_t) into direction (θ, ϕ) [2], [25]. A similar expression can be written for $\bar{S}(\pi - \theta, \phi)$ by replacing θ with $\pi - \theta$. Furthermore $\bar{K}(\theta)$ and $\bar{K}(\pi - \theta)$

are the upward and downward extinction coefficient matrices. For forest constituents with statistical azimuthal symmetry, the averages of the cross-polarized scattering amplitudes, $F_{mvh, mhu}$, vanish and the extinction matrix simplifies to (A4) at the bottom of the page. Where scattering amplitude tensor elements F_{mpp} (with $p = v, h$) are calculated in the forward direction for an exciting wave in direction (θ, ϕ) .

An approach to solve (A1) is to diagonalize the extinction matrices and then solve the resulting radiative transfer equations. This can be done using a matrix \bar{E} constructed from the eigenvectors of the extinction matrix [25]. For the matrix given in (A4) the eigenvector matrix is

$$\bar{E} = \frac{1}{2} \begin{bmatrix} 2 & 0 & 0 & 0 \\ 0 & 2 & 0 & 0 \\ 0 & 0 & 1 & j \\ 0 & 0 & 1 & -j \end{bmatrix}. \quad (A5)$$

Then by multiplying (A1) from the left-hand side by the matrix \bar{E} we can rearrange (A1) as

$$\begin{aligned} \cos \theta \frac{d\bar{I}(\theta, \phi, z)}{dz} &= -\bar{\kappa}(\theta) \bar{I}(\theta, \phi, z) + \bar{S}(\theta, \phi, z) \\ -\cos \theta \frac{d\bar{I}(\pi - \theta, \phi, z)}{dz} &= -\bar{\kappa}(\pi - \theta) \bar{I}(\pi - \theta, \phi, z) \\ &\quad + \bar{S}(\pi - \theta, \phi, z) \end{aligned} \quad (A6)$$

where

$$\begin{aligned} \bar{I}(\theta, \phi, z) &= \bar{E} \bar{I}(\theta, \phi, z) \\ \bar{\kappa}(\theta) &= \bar{E} \bar{K}(\theta) \bar{E}^{-1} \end{aligned} \quad (A7)$$

and

$$\begin{aligned} \bar{S}(\theta, \phi, z) &= \int_0^{2\pi} d\phi_t \int_0^{\pi/2} \sin \theta_t d\theta_t [\bar{Q}(\theta, \phi; \theta_t, \phi_t) \bar{I}(\theta_t, \phi_t, z) \\ &\quad + \bar{Q}(\theta, \phi; \pi - \theta_t, \phi_t) \bar{I}(\pi - \theta_t, \phi_t, z)] \end{aligned} \quad (A8)$$

$$\bar{Q}(\theta, \phi; \theta_t, \phi_t) = \sum_{m=1}^{N_1} n_m \bar{E} \langle \bar{P}_m(\theta, \phi; \theta_t, \phi_t) \rangle \bar{E}^{-1}. \quad (A9)$$

In (A7) $\bar{\kappa}(\theta)$ is a diagonalized matrix. Its elements are the eigenvalues of the extinction matrix \bar{K} . For the eigenvector

$$\begin{aligned} \bar{K}(\theta) &= \frac{2\pi}{k} \sum_{m=1}^{N_1} n_m \\ &\quad \begin{bmatrix} 2\text{Im}\langle F_{mvv} \rangle & 0 & 0 & 0 \\ 0 & 2\text{Im}\langle F_{mhh} \rangle & 0 & 0 \\ 0 & 0 & \text{Im}\langle F_{mvv} + F_{mhh} \rangle & \text{Re}\langle F_{mvv} - F_{mhh} \rangle \\ 0 & 0 & \text{Re}\langle F_{mhh} - F_{mvv} \rangle & \text{Im}\langle F_{mvv} + F_{mhh} \rangle \end{bmatrix}. \end{aligned} \quad (A4)$$

matrix given in (A5), see (A10) below. In addition, $\bar{I}(\theta, \phi, z)$ and $\bar{Q}(\theta, \phi; \theta_t, \phi_t)$ reduce to

$$\bar{I}(\theta, \phi, z) = \begin{bmatrix} I_v(\theta, \phi, z) \\ I_h(\theta, \phi, z) \\ \frac{1}{2}(I_3(\theta, \phi, z) + jI_4(\theta, \phi, z)) \\ \frac{1}{2}(I_3(\theta, \phi, z) - jI_4(\theta, \phi, z)) \end{bmatrix} \quad (\text{A11})$$

and (A12) at the bottom of the page. It is clear that the first two terms of the Stokes parameter vector (A11) do not change with the transformation.

Equations in (A6) are linear differential equations. For the purpose of iteration they can be written as integral equations in the form [34]

$$\begin{aligned} \bar{I}(\theta, \phi, z) &= e^{-\bar{\kappa}(\theta)(z+H_1)} \sec \theta \bar{I}(\theta, \phi, -H_1) \\ &\quad + \int_{-H_1}^z dz' e^{-\bar{\kappa}(\theta)(z-z')} \sec \theta \bar{S}(\theta, \phi, z') \\ \bar{I}(\pi - \theta, \phi, z) &= e^{\bar{\kappa}(\pi - \theta)z} \sec \theta \bar{I}(\pi - \theta, \phi, 0) \\ &\quad + \int_z^0 dz' e^{\bar{\kappa}(\theta)(z-z')} \sec \theta \bar{S}(\pi - \theta, \phi, z'). \end{aligned} \quad (\text{A13})$$

The zero-order solution of (A13) is obtained by setting the source function to zero yielding

$$\begin{aligned} \bar{I}^0(\theta, \phi, z) &= e^{-\bar{\kappa}(\theta)(z+H_1)} \sec \theta \bar{I}^0(\theta, \phi, -H_1) \\ \bar{I}^0(\pi - \theta, \phi, z) &= e^{\bar{\kappa}(\pi - \theta)z} \sec \theta \bar{I}^0(\pi - \theta, \phi, 0) \end{aligned} \quad (\text{A14})$$

where $\bar{I}^0(\theta, \phi, -H_1)$ and $\bar{I}^0(\pi - \theta, \phi, 0)$ are to be obtained from the boundary conditions. The v th order solution ($v > 1$) can be written as

$$\begin{aligned} \bar{I}^v(\theta, \phi, z) &= \int_{-H_1}^z e^{-\bar{\kappa}(\theta)(z-z')} \sec \theta \bar{S}^v(\theta, \phi, z') \\ \bar{I}^v(\pi - \theta, \phi, z) &= \int_z^0 e^{\bar{\kappa}(\theta)(z-z')} \sec \theta \bar{S}^v(\pi - \theta, \phi, z') \end{aligned} \quad (\text{A15})$$

with

$$\begin{aligned} \bar{S}^v(\theta, \phi, z') &= \int_0^{2\pi} d\phi_t \int_0^{\pi/2} \sin \theta_t d\theta_t [\bar{Q}(\theta, \phi; \theta_t, \phi_t) \bar{I}^{v-1}(\theta_t, \phi_t, z') \\ &\quad + \bar{Q}(\theta, \phi; \pi - \theta_t, \phi_t) \bar{I}^{v-1}(\pi - \theta_t, \phi_t, z')]. \end{aligned} \quad (\text{A16})$$

The original Stokes parameters can be recovered from (A14) and (A15) by multiplying them by \bar{E}^{-1} .

REFERENCES

- [1] G. M. Woodwell, *The Role of Terrestrial Vegetation in the Global Carbon Cycle: Measurement by Remote Sensing*, New York: Wiley, 1984.
- [2] F. T. Ulaby, R. K. Moore, and A. K. Fung, *Microwave Remote Sensing: Active and Passive*, vol. I. New York: Addison-Wesley, 1981, vol. II. New York: Addison-Wesley, 1984, vol. III. Dedham, MA: Artech House, 1986.
- [3] A. J. Sieber, "Forest signatures in imaging and nonimaging microwave scatterometer data," *ESAJ*, vol. 9, pp. 431-448, 1985.
- [4] H. Hirose, Y. Matsuzaka, and O. Kobayashi, "Measurement of microwave backscatter from a Cypress with and without leaves," *IEEE Trans. Geosci. Remote Sensing*, vol. 27, pp. 698-701, 1989.
- [5] D. E. Pitts, G. D. Badhwar, and E. Reyna, "The use of a helicopter mounted ranging scatterometer for estimating of the extinction and scattering properties of forest canopies, part II, experimental results for high density aspen," *IEEE Trans. Geosci. Remote Sensing*, vol. 26, pp. 144-151, 1988.
- [6] S. T. Wu, "Preliminary report on measurements of forest canopies with C-band radar scatterometer at NASA/NSLT," *IEEE Trans. Geosci. Remote Sensing*, vol. GE-24, pp. 894-899, 1986.
- [7] R. Zoughi, L. W. Wu, and R. K. Moore, "Identification of major backscattering sources in trees and shrubs at 10 GHz," *Remote Sensing of Environment*, vol. 19, pp. 269-290, 1986.
- [8] E. Mougin, A. Lopes, and T. LeToan, "Microwave propagation at X band in cylindrical shaped forest components: Attenuation observations," *IEEE Trans. Geosci. Remote Sensing*, vol. 28, pp. 60-69, 1990.
- [9] D. M. Le Vine, A. Schneider, R. H. Lang, and H. G. Carter, "Scattering from thin dielectric disks," *IEEE Trans. Antennas Propagat.*, vol. AP-33, pp. 1410-1413, 1985.
- [10] N. Engheta and C. Elachi, "Radar scattering from a diffuse vegetation layer over a smooth surface," *IEEE Trans. Geosci. Remote Sensing*, vol. GE-20, pp. 212-216, 1982.
- [11] J. A. Richards, G.-Q. Sun, and D. S. Simonett, "L-band radar backscatter modeling of forest stands," *IEEE Trans. Geosci. Remote Sensing*, vol. GE-23, pp. 487-498, 1987.
- [12] S. L. Durden, J. J. Van Zyl, and H. A. Zebker, "Modeling and observation of radar polarization signature of forested areas," *IEEE Trans. Geosci. Remote Sensing*, vol. 27, pp. 290-301, 1989.
- [13] F. T. Ulaby, K. Sarabandi, K. McDonald, M. Whitt, and M. C. Dobson, "Michigan Microwave canopy scattering model," *Int. J. Remote Sensing*, vol. 11, no. 7, pp. 1223-1253, 1990.
- [14] K. C. McDonald, M. C. Dobson, and F. T. Ulaby, "Using MIMICS to model L-Band Multiangle and multitemporal backscatter from a walnut orchard," *IEEE Trans. Geosci. Remote Sensing*, vol. 28, pp. 477-491, 1990.
- [15] K. C. McDonald, M. C. Dobson, and F. T. Ulaby, "Modeling multi-frequency diurnal backscatter from a walnut orchard," *IEEE Trans. Geosci. Remote Sensing*, vol. 29, pp. 852-863, 1991.
- [16] M. A. Karam and A. K. Fung, "Scattering from randomly oriented circular discs with application to vegetation," *Radio Sci.*, vol. 18, pp. 557-563, 1983.

$$\bar{\kappa}(\theta) = \frac{2\pi}{k} \sum_{m=1}^{N_1} n_m \begin{bmatrix} 2\text{Im}\langle F_{m\nu\nu} \rangle & 0 & 0 & 0 \\ 0 & 2\text{Im}\langle F_{mhh} \rangle & 0 & 0 \\ 0 & 0 & \text{Im}\langle F_{m\nu\nu} + F_{mhh} \rangle & 0 \\ 0 & 0 & +j\text{Re}\langle F_{m\nu\nu} - F_{mhh} \rangle & \text{Im}\langle F_{m\nu\nu} + F_{mhh} \rangle \\ & & & -j\text{Re}\langle F_{m\nu\nu} - F_{mhh} \rangle \end{bmatrix}. \quad (\text{A10})$$

$$\bar{Q}(\theta, \phi; \theta_s, \phi_s) = \sum_{m=1}^{N_1} n_m \begin{bmatrix} \langle |F_{m\nu\nu}|^2 \rangle & \langle |F_{m\nu h}|^2 \rangle & \langle F_{m\nu\nu} F_{m\nu h}^* \rangle & \langle F_{m\nu\nu}^* F_{m\nu h} \rangle \\ \langle |F_{m h\nu}|^2 \rangle & \langle |F_{m h h}|^2 \rangle & \langle F_{m h\nu} F_{m h h}^* \rangle & \langle F_{m h\nu}^* F_{m h h} \rangle \\ \langle F_{m\nu\nu} F_{m h\nu}^* \rangle & \langle F_{m\nu h} F_{m h h}^* \rangle & \langle F_{m\nu\nu} F_{m h h}^* \rangle & \langle F_{m\nu h} F_{m h h}^* \rangle \\ \langle F_{m\nu\nu}^* F_{m h\nu} \rangle & \langle F_{m\nu h}^* F_{m h h} \rangle & \langle F_{m\nu h} F_{m h\nu}^* \rangle & \langle F_{m\nu h}^* F_{m h h} \rangle \end{bmatrix} \quad (\text{A12})$$

- [17] M. A. Karam and A. K. Fung, "Scattering from randomly oriented scatterer of arbitrary shape in the low frequency limit with application to vegetation," *Digest of Intr. Geosci. Remote Sensing Sym.* (IGARSS'83) pp. 2:5.1-5.7, 1983.
- [18] M. A. Karam and A. K. Fung, "Electromagnetic scattering from a layer of finite randomly oriented, dielectric, circular cylinders over a rough interface with application to vegetation," *Int. J. Remote Sensing*, vol. 9, no. 6, pp. 1109-1134, 1988.
- [19] H. J. Eom and A. K. Fung, "Scattering from a random layer embedded with dielectric needles," *Remote Sensing of Environment*, vol. 19, pp. 139-149, 1986.
- [20] A. K. Fung, M. F. Chen, and K. K. Lee, "Fresnel field interaction applied to scattering from a vegetation layer," *Remote Sensing of Environment*, vol. 23, pp. 35-50, 1987.
- [21] R. H. Lang and J. Sidhu, "Electromagnetic from a layer of vegetation: a discrete approach," *IEEE Trans. Geosci. Remote Sensing*, vol. GE-21, pp. 67-71, 1983.
- [22] N. S. Chauhan, R. H. Lang, and K. J. Ranson, "Radar modeling of a Boreal Forest," *IEEE Trans. Geosci. Remote Sensing*, vol. 29, pp. 627-638, 1991.
- [23] H. T. Chuah, and H. S. Tan, "A multiconstituent and multilayer microwave backscatter model for a vegetation medium," *Remote Sensing of Environment*, vol. 31, pp. 137-153, 1990.
- [24] A. K. Fung, and H. S. Fung, "Application of first order renormalization method to scattering from a vegetation-like half space," *IEEE Trans. Geosci. Remote Sensing*, vol. GE-15, pp. 189-195, 1977.
- [25] L. Tsang, J. A. Kong, R. T. Shin, *Theory of Microwave Remote Sensing*. New York: John Wiley & Sons, 1985, pp. 139-140.
- [26] J. Cimino, M. C. Dobson, D. Gates, E. Kasischke, R. Lang, J. Norman, J. Paris, F. T. Ulaby, S. Ustin, V. Vanderbilt, and J. Weber, "EOS synergism study 1987 field experiment data report," JPL Tech. Rep., May 1988.
- [27] M. A. Karam, A. K. Fung, and Y. M. M. Antar, "Electromagnetic wave scattering from some vegetation samples," *IEEE Trans. Geosci. Remote Sensing*, vol. 26, pp. 799-808, 1988.
- [28] S. S. Seker and A. Schneider, "Electromagnetic scattering from a dielectric cylinder of finite length," *IEEE Trans. Antennas Propagat.*, vol. 36, pp. 303-307, 1988.
- [29] M. A. Karam and A. K. Fung, "Leaf-shape effects in electromagnetic wave scattering from vegetation," *IEEE Trans. Geosci. Remote Sensing*, vol. 27, pp. 687-697, 1989.
- [30] M. Abramowitz and I. A. Stegun, *Handbook of Mathematical Functions*. New York: Dover Publications, Inc., 1972, pp. 887-920.
- [31] F. T. Ulaby and M. A. El-Rayes, "Microwave Dielectric spectrum of vegetation part II: Dual dispersion model," *IEEE Trans. Geosci. Remote Sensing*, vol. 25, pp. 550-557, 1987.
- [32] A. Lopes, E. Mougin, T. LeToan, M. A. Karam, and A. K. Fung, "A simulation study on the influence of leaf orientation on elliptically polarized microwave propagation in a coniferous forest," *J. Electromagnetic Waves and Applications*, vol. 5, no. 7, pp. 753-776, 1991.
- [33] E. Mougin, A. Lopes, M. A. Karam, and A. K. Fung, "Effect of tree structure on X-Band microwave signature of conifers," *IEEE Trans. Geosci. Remote Sensing*, Submitted for publication, 1991.
- [34] M. A. Karam and A. K. Fung, "Propagation and scattering in multi-layered random media with rough interfaces," *Electromagnetics*, vol. 2, pp. 239-256, 1982.



Mostafa A. Karam (M'81-SM'90) received the B.Sc. degree (with first honor) and the M.Sc. degree, both in electrical engineering, from Cairo University, Giza, Egypt, in 1977 and 1980, respectively. He received the Ph.D. degree in electrical engineering from the University of Kansas, Lawrence, KS in 1984.

During the period 1977-1980, he worked as a teaching assistant at Cairo University. He was with the Remote Sensing Laboratory at the University of Kansas as an Assistant Project Engineer, from

1980-1984. He has been with the Wave Scattering Research Center at the University of Texas at Arlington as a research associate since 1984. He authored or coauthored a number of publications on applied electromagnetics, waves in random media, and microwave remote sensing. His recent research interests include forest polarimetric signatures, interference in radio wave communication systems due to scattering from earth terrain, and land surface-atmosphere interaction and its roles in global change.

Dr. Karam is a co-Founder and the present Chairman of IEEE Antennas and Propagation Society, Fort Worth Chapter. He is a member of the Electromagnetic Academy and is listed in Who's Who in Electromagnetics in 1990.



Adrian K. Fung (S'60-M'66-SM'70-F'85) received the B.S. degree from Cheng Kung University, Taiwan, China in 1958, the M.S.E.E. degree from Brown University, Providence, RI in 1961, and the Ph.D. degree from the University of Kansas, Lawrence, KS, in 1965.

From 1965-1984 he was on the faculty of the Department of Electrical Engineering, University of Kansas. In the fall of 1984 he joined the University of Texas at Arlington where he is now a professor with the Electrical Engineering Department and

Director of the Wave Scattering Research Center. His research interests have been in the areas of radar wave scattering and emission from earth terrains and sea, and radar and ISAR image generation, simulation, and interpretation. He has contributed to many book chapters and is a coauthor of the three-volume book on *Microwave Remote Sensing* (Artech House, vol. 1, 1981; vol. 2, 1982; vol. 3, 1986). He has served as an Associate Editor of *Radio Science* and *IEEE JOE*.

Dr. Fung was the recipient of the Halliburton Excellence in Research Award in 1986, the 1989 Distinguished Research Award of the University of Texas at Arlington and the 1989 Distinguished Achievement Award from the IEEE Geoscience and Remote Sensing Society. He is a member of IEEE.



Roger H. Lang (S'66-M'68-SM'86-F'89) received the B.S. and M.S. degrees in electrical engineering in 1962 and 1964, respectively, and the Ph.D. degree in electrophysics in 1968, all from the Polytechnic University of Brooklyn, NY.

He worked at Bell Telephone Laboratories on satellite antennas during 1963-1964, and he did postdoctoral work on wave propagation in random media at the Courant Institute of Mathematical Sciences of New York University during 1969-1970 before joining George Washington University, Washington, DC. He now holds the position of Professor in the Department of Electrical Engineering and Computer Science at GWU and during the period 1984-1988 he served as Department Chairman. He has worked with NASA's Land Processes Group in developing microwave discrete scattering models of vegetation. Professor Lang has been an active participant in the IEEE Geoscience and Remote Sensing Society for whom he is presently the Associate Editor for Microwave Scattering and Propagation and a member of the Society's Administrative Committee. He was Co-Chairman of the Technical Program Committee for the IGARSS'90 meeting held at College Park, MD, in 1990.

Dr. Lang is a member of IEEE.



Narinder S. Chauhan (M'87) received the M.Sc. degree in physics, the M.E. degree (Honors) in computer science, and the Ph.D. degree in space physics from Punjabi University, India, in 1972, 1983, and 1979, respectively.

He is currently working for USRA in the Hydrological Sciences Branch at NASA's Goddard Space Flight Center, Greenbelt, MD. His research is focused on the application of microwave models for active and passive remote sensing of vegetation.

Prior to joining GSFC, he was teaching in the Department of Electrical Engineering and Computer Sciences at the George Washington University, Washington, DC, where his research interests were in inverse problems of remote sensing and microwave modeling the radar scattering from vegetation especially the forest canopies. In early part of his career, he also worked on theoretical modeling of ionosphere in a collaborative effort with AFGL, Cambridge. He is a member of the IEEE Geoscience and Remote Sensing Society.

Dr. Chauhan is a member of IEEE and AGU.

To: Denise Dunn, Administrative Assistant, USRA
 From: Steven W. Bidwell, Task No. 970-023
 Subject: Quarterly Report (July 1, 1992 - September 30, 1992)
 Date: 11/12/92

August 3, 1992 was the date of my hire in association with the Microwave Sensors Branch (Code 975) of the Laboratory for Hydrospheric Processes. The following is a narrative report on my activities during the past quarter-year presented in chronological order.

Soon after my hiring I made one short overnight 8/5 - 8/6 trip to Wallops Island, VA. During this trip I gained a cursory experience with the millimeter-wave imaging radiometer (MIR) experiment. I became acquainted with the overall system and its integration into the ER-2 aircraft. Paul Racette of Code 975 is the lead engineer on this program and whenever possible I have lent assistance. In this effort I spent about 1.5 weeks working on a gray-scale plotting routine for the MIR data. This routine displays pixel brightness temperature data on a gray-scale hard copy.

The majority of my efforts have been devoted to the EDOP (ER-2 DOPpler radar) experimental radar program. Dr. Gerald Heymsfield of Code 912 (Severe Storms Branch) is the Principal Investigator for this program. There is a critical need for a systems engineer on this program and one of my responsibilities is to fill this role. The EDOP airborne radar system is composed of various subsystems: transmitter, receiver, power distribution, aircraft interface, cabling, waveguide and antennas, and data system. My prior experience in microwave tubes has aided in the troubleshooting of the transmitter and receiver systems. However, numerous problems remain with the data acquisition system and its interface with the radar. My digital electronics experience with regard to the data system is not as comprehensive. It is my goal as the systems engineer to obtain a "jack-of-all-trades" knowledge of the various subsystems.

For a two week period in September 9/15 - 9/26 I was on travel to the Ames Research Center at Moffat Field, CA with Dr. Gerald Heymsfield and the EDOP group. The purpose of this trip

was to fly the Doppler radar system aboard the ER-2 aircraft, gather data, and eliminate remaining problems. Presently the EDOP program is preparing for the ocean and atmospheric experiments in the Southwest Pacific (TOGA-COARE) during January and February 1993. The flights at Ames are intended to ready the EDOP system for this upcoming mission. Largely my time at Ames was spent on troubleshooting the radar and identifying potential failure modes.

In addition to the EDOP activities I have been investigating the possible use of the MIR data from the TOGA-COARE experiments to examine cloud physics. (The MIR is also involved in the TOGA-COARE mission). The MIR device collects brightness temperatures at nine millimeter-wave frequencies. Using data from the 183 GHz and 325 GHz channels one might make some cloud physics observations. Specifically, the two frequencies of interest are water vapor absorption lines and through knowledge of the brightness temperature weighting functions at these frequencies one might estimate the vertical extent of clouds. This would provide an alternative method to a more conventional means using radar.

Finally, in collaboration with Drs. James Weinman and Wei-Kao Tao, I have submitted a Director's Discretionary Fund Proposal to examine processing techniques for a spatial imaging enhancement of radiometric signals. These techniques will be dependent upon over sampling of the desired scene. Such a technique, using a numerical filter, might be used on the TRMM (Tropical Rainfall Measuring and Monitoring) satellite mission. If not applied to this mission, it might be used on the ESTAR (Electronically Scanned Thinned Array Radiometer) satellite. If this proposal is successful I will examine resolution enhancement techniques from data obtained from the MIR experiment. I will intentionally blur the scene and attempt recovery using various numerical techniques. A scene involving a sharp spatial transition such as a coastline might be used in these studies.

For the next quarter year most of my effort will again be concentrated on producing a successful EDOP program. Tests flights at Ames Research Center are planned for mid-November and mid-December. When not working on this program, I will be investigating the scientific programs mentioned above (MIR data for cloud physics and the DDF proposal on resolution enhancement).

970-021

Quarterly Technical Report
July 1, 1992 - September 30, 1992
Dr. A. Daniel Kowalski
Task# 970027

1 Introduction

My primary research activity is concerned with the development of algorithms and corresponding programs for high performance numerical modeling of coupled ocean - atmosphere circulation. These algorithms must be scalable to run on future massively parallel machines containing thousands of processors and capable of teraFLOP performance. This involves spatial and/or functional decomposition of algorithms along with corresponding data dependency analysis.

The research also involves a detailed performance analysis of different parallel machine architectures. Machine details like, for example, the presence of instruction and data cache, vector processing units, pipelined instruction hardware, and interprocessor communication architecture can greatly affect algorithm performance.

2 Research Activities for the Period July 1, 1992 to September 30, 1992

I Co-authored a NASA NRA hpcc proposal with Dr. Max Suarez and Dr. Paul Schopf of NASA/GSFC entitled "Development of Algorithms for Climate Models Scalable to Teraflop Performance". The proposal is still pending. In addition, I composed and submitted a successful mini-proposal for computer time on the INTEL Touchstone DELTA parallel computer at Caltech. I also composed a proposal section for NCCS for a project which would run a coupled atmosphere-ocean model using a distributed system of supercomputers coupled by high speed satellite communications.

Computational work has included conducting single and multiple node performance measurements on the Intel Touchstone Delta and CRAY Y-MP at NASA/GSFC with benchmarks derived from the Goddard coupled ocean/atmosphere model. The benchmarks include the long wave radiation code from the Aries atmospheric model and momentum and continuity hydrodynamics code from the Poseidon ocean model. Current results indicate 2-3 Mflop performance per node on the Touchstone Delta with optimized but untuned benchmark code and 200 Mflop Cray single node performance.

Other activities include the submission of an abstract for the 6th SIAM Conference on Parallel Processing for Scientific Computing and attendance at the Frontiers '92 Conference on Massively Parallel Computation.

3 Planned Activities for the 4th Quarter July 1, 1992 to September 30, 1992

During the next quarter, I plan to continue speedup and efficiency tests on developed benchmarks as well as continue the development and testing of new parallel algorithms for the coupled ocean/atmospheric model. This will begin with the development of a parallel short wave radiation code for the atmospheric model.

I also plan to write a paper for the 6th SIAM Conference on Parallel Processing for Scientific Computing and a workshop on High Performance Computing in the Geosciences.

CC1 1 3 16

of data will be performed by comparing the resulting fraction images with the classification derived from TM/Landsat and AVHRR NDVI images.

STUDY SITE

The study site is located between 17° 50' to 18° 20' South latitude and 52° 40' to 53° 20' West longitude on the border of Goiás, Mato Grosso and Mato Grosso do Sul States. The site includes the Emas National Park comprising about 131,000 hectares in which the "cerrado" vegetation is well represented (Redford 1985, IBDF/FBCN 1978, Pinto 1986). Located on the watershed between the La Plata and Amazon River basins, Emas Park is on the western edge of the Central Brazilian Plateau, adjacent to the Pantanal (Redford 1985). It offers a good sample of the Planalto habitats, including a number of small watercourses, the sources of two important rivers, riverine gallery forest and marshes, large areas of grassland (the "campos"), and some open woodland (the "cerrados") consisting of small thinly distributed trees seldom more than three meters high (Erize 1977). The surrounding land of the Park has been used for agricultural and cattle grazing. This Park is commonly affected by uncontrolled fires during the annual dry season (Shimabukuro et al. 1991). Most of these fires are set outside the Park by ranchers to improve grazing quality and to control cattle parasites (Redford 1985). The rest of the study site is covered by "cerrado" vegetation types. The Landsat/TM and NOAA/AVHRR data over this area acquired on July 29, 1988 were available for this study.

METHOD

AVHRR 3.75 μm Reflective Component

The AVHRR 3.75 μm band is a mixture of the thermal emitted energy and a reflective energy component. Typically the latter represents less than 10% of the signal for bare soil and urban features and less than 3 percent for green vegetation (Kerber and Schutt 1986; and Schutt and Holben 1991; Remer 1992). The reflective component may be approximated by assuming the emitted energy (brightness temperature) in the adjacent thermal band (10.5 to 11.5 μm) is related to the emitted energy in the 3.75 μm band at ambient temperature through the Planck Function as follows (Kaufman and Nakajima 1992):

$$L_3 = L_{3\rho} + L_{3\varepsilon} \quad (1)$$

where:

L_3 = Total radiant energy measured by the satellite at 3.75 μm

$L_{3\rho}$ = The reflective energy at 3.75 μm

$L_{3\varepsilon}$ = The emissive energy at 3.75 μm

The reflective and emitted components may be expanded according to:

$$L_3 = \rho_3 F_0 \mu_0 / \pi + R_3(T_4) * (1 - \rho) \quad (2)$$

where:

ρ_3 = Reflectance in the 3.75 μm band

F_0 = 3.75 band solar irradiance at the bottom of the atmosphere

μ_0 = cosine of the solar zenith angle

$R_3(T_4)$ = Emitted radiance at 3.75 μm using the 11.0 μm brightness computed with the Planck Function

Solving for ρ_3 :

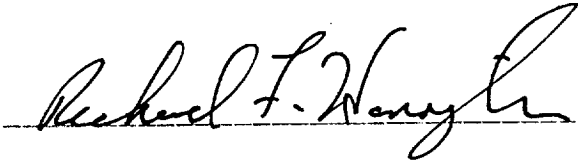
$$\rho_3 = (L_3 - R_3(T_4)) / (F_0 \mu_0 / \pi - R_3(T_4)) \quad (3)$$

This formulation ignores the differential atmospheric transmission in both bands and we assume the target surface is flat and the satellite view direction is nadir.

August 24, 1992

MEMORANDUM

TO: Denise Dunn, USRA

FROM: Dr. Richard F. Harrington SUBJECT: Trip Report: Goddard Space Flight Center, Greenbelt Maryland
August 20 & 21, 1992

Dr. James C. Shiue of GSFC requested that I visit him at GSFC on August 20 & 21, 1992 to review the TRMM Microwave Imager (TMI) Conceptual Design Review (CoDR) data package. This meeting was in preparation for the TMI CoDR to be held at the Hughes facility in Los Angeles on August 26 & 27, 1992. Dr. Shiue had requested on Monday August 17 that I look into two areas of technical concern prior to the GSFC meeting later in the week.

The two areas of concern were:

- (a) Undersampling of the 85.5 GHz channel and the desirability of increasing the TMI scan rate to improve the sampling rate of the scene; and
- (b) the use of a 12 bit A/D converter with AGC in lieu of the specified 14 bit A/D converter without AGC.

The meeting on Tuesday afternoon, August 20th, was held with Dr. Shiue and the above two items were discussed. Also, the TMI CoDR data package was obtained from Dr. Shiue. This was reviewed during that evening in preparation for the discussion on Friday with Dr. Shiue.

The meeting on Friday, August 21st, was held with Dr. Shiue. Detailed discussions on many aspects of the TMI CoDR data package were held. These discussions included, but not limited to the following items:

- (a) The use of integrate and dump techniques as compared to low pass filtering for the integration of the scene in the radiometer design.
- (b) Why is Aerojet using a 14 bit A/D converter in the SSMIS design in lieu of a 12 bit A/D converter with AGC?
- (c) Effect of the A/D converter and low pass filtering on the pixel-to-pixel interference specification.
- (d) Question of possible interference from the precipitation radar (PR) into the TMI's 10.65 GHz channel. Related experience from the Seasat spacecraft and the interference of the SASS into the 6.6 and 10.6 GHz channels of the SMMR.
- (e) Cold sky reflector orientation with respect to the spacecraft.
- (f) Undersampling effects at 85.5 GHz

The meeting was concluded with discussion of the information Dr. Shiue needed prior to the TMI CoDR. Also, Dr. Shiue requested that I take notes during all technical discussions during the CoDR.

MEMORANDUM

August 7, 1992

TO: Dr. James C. Shiue
Goddard Space Flight Center
Greenbelt, Md.

FROM: Dr. Richard F. Harrington *RFH*
Old Dominion University
Norfolk, VA.

SUBJECT: Potential technical problem for the TRMN Microwave Imager.

STATEMENT OF PROBLEM

The Precipitation Radar (PR) and the TRMN Microwave Imager (TMI) are operating simultaneously during the TRMN mission. The TMI measures the total electromagnetic (EM) energy incident at the input of the radiometer during one integration period. The TMI can not differentiate between the EM energy radiated from the geophysical phenomena such as liquid water in rain which is used to determine rain rate and the coherent EM energy that leaks into the radiometer while the PR is transmitting. Therefore the TRMN system design must insure that the level of PR leakage is sufficiently below the threshold or sensitivity of the TMI to insure minimal error due to the PR leakage radiation.

Microwave radiometers typically use waveguide inputs from the antenna to the low noise amplifier (LNA), if used, or the mixer preamplifier if no LNA is employed. A waveguide is a high-pass filter which only passes EM energy whose frequency is above the cut-off frequency of the waveguide. Therefore spacecraft systems in which the radar operates at a frequency lower than the cut-off frequency of the radiometer input waveguide usually have sufficient isolation within the waveguide structure. This is the case for the 19.35, 22.235, 37 and 85.5 GHz channels of the TMI. The 13.8 GHz frequency of the PR is below the 14.09 GHz cut-off frequency for the 19.35 and 22.235 GHz channels of the TMI. However, the 13.8 GHz frequency of the PR is above the frequency of the 10.65 GHz channel of the TMI. It will be shown later in this memorandum that a total isolation of 165.3 dB is required to insure that the EM radiation from the PR is equal to one-tenth of the EM radiation required for an output of 0.5 Kelvin from the TMI.

POTENTIAL PROBLEM SOLUTIONS

There are two potential solutions to the above problem:

- (1) Disable the TMI during the PR transmitting time thru the use of a blanking pulse from the PR.
- (2) Provide sufficient isolation by techniques both internal and external to the TMI. A bandstop filter can be added within the RF frontend of the 10.65 GHz channel of TMI. External isolation can be obtained through location of the PR and TMI antennas and detailed analysis of antenna sidelobes.

The first solution is highly desirable since it guarantees a solution to this problem by design. However, it requires an interface between the PR and TMI, a design change in the existing TMI, and potentially an additional output from the PR.

The second solution requires a high level of isolation between the PR and TMI antennas. To insure that the TRMN spacecraft system design provides

(2)

sufficient isolation is a difficult and complicated analytical problem. Testing of the PR antenna and TMI on a spacecraft mockup would be required very early in the program to allow sufficient time for redesign. If sufficient isolation could not be obtained, then a redesign of the PR and TMI could be required.

ISOLATION REQUIREMENT CALCULATION

- (1) PR Parameters: Frequency: 13.796 and 13.802 GHz.
Peak Power: 500 Watts
Pulse Width: 1.67 microseconds
Pulse Repetition Frequency: 2778.3 pulses per second
- (2) TMI 10.65 GHz Channel Parameters: Frequency: 10.65 GHz.
RF Bandwidth: 100 MHz.
Integration Time: 30.67 milliseconds
Required Radiometer Sensitivity: 0.5 K

Step 1: Determine the increase or delta in the electromagnetic (EM) energy required at the input to the TMI to increase the output by 0.5 K during one integration period.

delta energy = delta power X integration time

delta power = k X sensitivity X bandwidth

where k = Boltzman's constant = 1.38×10^{-23} Joules/Kelvin
sensitivity = 0.5 Kelvin
bandwidth = 100 MHz
integration time = 30.67 milliseconds

delta energy = $(1.38 \times 10^{-23})(0.5)(1 \times 10^8)(30.67 \times 10^{-3})$

delta energy = 2.116×10^{-17} Joules

Step 2: Determine the electromagnetic (EM) energy radiated by the PR during one integration time of the 10.65 GHz channel of TMI.

PR energy = Peak power X Pulsewidth X PRF X Integration time

PR energy = $(500)(1.67 \times 10^{-6})(2778.3)(30.67 \times 10^{-3})$

PR energy = 7.115×10^{-2} Joules

Step 3: Determine the isolation required.

ASSUMPTION: To prevent the PR energy from increasing the TMI output, the PR energy must be 1/10 of the energy required to give an output of 0.5 Kelvin from the 10.65 GHz channel of the TMI. Therefore:

PR energy must be equal to or less than 2.116×10^{-18} Joules.

ISOLATION = $10 \log(7.115 \times 10^{-2} / 2.116 \times 10^{-18})$

ISOLATION = 165.3 dB

(3)

Since the bandpass filter in the TMI is specified to provide 40 dB of attenuation to out-of-band EM signals, the total required isolation between the PR antenna and the TMI antenna for minimum error due to leakage from the PR is:

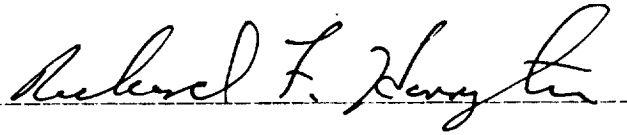
ANTENNA ISOLATION = 125.3 dB or greater

August 31, 1992

MEMORANDUM

TO: Denise Dunn, USRA

FROM: Dr. Richard F. Harrington



SUBJECT: Trip Report: Hughes Aircraft Company, El Segundo, CA August 25 thru 28, 1992

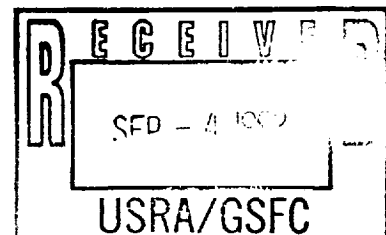
Dr. James C. Shiue of GSFC requested that I attend the TRMM Microwave Imager (TMI) Conceptual Design Review (CoDR) that was held at the Hughes Aircraft Company facility in El Segundo, CA as a member of the TMI Technical Advisory Group. A detailed listing of the discussion items is provided in the attached memorandum to Dr. Shiue dated August 31, 1992. A list of the attendees at the CoDR is also attached. Material obtained at the CoDR included updates to the TMI CoDR data packages and Hughes Interdepartmental Correspondance from Jamie Hilleary, who was unable to attend the CoDR. A tour of the microwave testing laboratory and a demonstration of the two frequency linearity test set-up was conducted Tuesday evening by Dr. Victor Reinhardt of Hughes.

The CoDR was very successful and demonstrates the excellant communications that exists between the GSFC TRMM project office and the TMI contractor, Hughes Aircraft Company.

Members of Dr. Shiue's TMI Technical Advisory Group that attended the TMI CoDR included:

- Dr. James C. Shiue - GSFC TMI Instrument Scientist
- Dr. Wes Lawrence - NASA Langley
- Dr. James Hollinger - Naval Research Laboratory
- Dr. Richard F. Harrington - Old Dominion University

Also in attendance representing the TMI science team was Dr. Tom Wilheit of Texas A & M University.

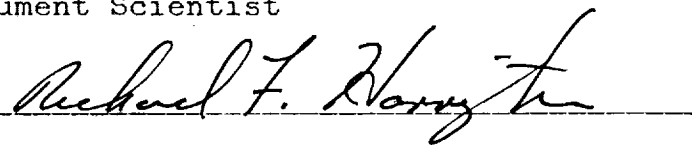


August 31, 1992

MEMORANDUM

TO: Dr. James C Shiue, TMI Instrument Scientist
GSFC

FROM: Dr. Richard F. Harrington
Old Dominion University



SUBJECT: TMI CoDR discussion items requiring further study and/or action.

The following is a tabulation of items requiring further study or actions. These items are from my notes taken during the TRMM Microwave Imager (TMI) Conceptual Design Review (CoDR) held at the Hughes Aircraft Company facility in El Segundo, CA on August 26 & 27, 1992.

(1) The linearity specification is very tight and overall system testing can not be accomplished to demonstrate compliance with the specification. Subsystem level testing and analysis will have to be performed to show that the linearity requirement has been met.

(2) Change of polarization at 22.235 GHz from vertical to horizontal.

(3) Change of frequency from 22.235 GHz to 21.3 GHz.

(4) The Mil-Std 1773 bus with the 1553 protocol is new to both Hughes and GSFC. Question of the lack of experience which might result in unforeseen problems in the design phase which only show up in testing. What NASA flight programs have been designed, fabricated, tested and flown using the Mil-Std 1773 bus and 1553 protocol?

(5) Reduction of the 140 degree scan angle to 130 degrees and the resulting impact on the swath width?

(6) Potential of using direct detection at 85.5 GHz. Need to study the maturity of components such as LNA's at this frequency prior to a decision to use direct detection at 85.5 GHz.

(7) PR interference with the 10.65 GHz, 19.35 GHz and 22.235 GHz channels of the TMI. Need to document results of splinter group meeting. Hughes took an action item to solve this problem thru design.

(8) Mechanical interference of TMI during deployment. Further study by Hughes and GSFC is needed to insure that there is not a problem with the recommended deployment option, option C.

(9) Cold sky reflector might see a portion of the spacecraft/solar panels. What is the impact of reducing the scan angle from 140 degrees to 130 degrees? Calculation and/or measurements of potential cold sky calibration error needs to be in the future TMI planning. A 1% spacecraft view of a 300 K spacecraft introduces a 100 % error in the cold sky measurement.

(10) Post detection integration can be achieved either by low-pass filtering or integrate and dump circuits. In the undersampling scheme designed into TMI, which is the correct technique?

- (11) Spin-speed study to improve sampling and provide contiguous coverage at 85.5 GHz. Note: I did not cover this splinter meeting since I was involved in the PR - TMI interference splinter meeting.
- (12) Momentum wheel - questions on:
- (a) physical location
 - (b) input power from raw spacecraft bus
 - (c) design of electronics and control loop
 - (d) when is the BAPTA slaved to the momentum wheel and when is BAPTA slaved to the crystal reference?
 - (e) thermal environment of momentum wheel.
- (13) Atomic oxygen specification, is it excessive?
- (14) Question of the gain drift of the direct detection radiometer receivers as a function of temperature, age and voltage. Is the AGC system dynamic range, resolution and the 12 bit A/D convertor capable of accomodating these expected variations. Note: This is a totally different receiver design from SSM/I.
- (15) Cold sky calibration accuracy of 0.2 K is not achievable. Is this over specified and should it be relaxed?
- (16) How is proper TMI deployment verified from spacecraft telemetry prior to spin-up of the TMI? Is this information needed?
- (17) Data load of 42 Kbps as compared to 37 Kbps due to adding 4 zero bits to 12 bit data to make a 16 bit word required for the Mil-Std 1773 requirement. Should revised data packing and/or data compression be employed to reduce the data load requirement?
- (18) Hughes would like to format 1 scan of data as compared to the GSFC requirement to format 3 scans of data.
- (19) Automatic gain control, questions concerning time period of adjustment, dynamic range and step size using a 4 bit AGC word?
- (20) Torque margin, difference between the Hughes position on acceptable torque margin as compared to the four times worst case required by GSFC.
- (21) Stability of spacecraft supplied clocks and their effect on TMI performance.
- (22) Ephemeris error was missing from pointing error budget.
- (23) Implementation of redundancy in optical transmitters and receivers in the Mil-Std 1773 bus. Use of OR circuit. Is data being sent out simultaneously on both buses? Are both receivers active? Need better definition and understanding on the MIL-Std 1773 bus design.
- (24) Question of SEU performance requirement. How is detection of a single event accomplished? How is the recovery from a single event achieved? Confusion on specification and potential solutions.
- (25) The pointing error of the 10.65 GHz channel beam of 0.2 degrees is relative to the position of the multifrequency SSM/I horn which is 0.2 degrees relative to the 49 degree requirement. This needs a clarification in the specification.

(3)

(26) Spillover effects of the cold sky feed horn on the accuracy of cold sky calibration. Hughes accepted an action item to study this problem.

(27) Hughes requested that the power supply frequencies be increased from the GSFC requirement of 50 KHz maximum to 200 KHz maximum.

(28) Difference in the thermal interface specification:

(a) GSFC: -25 deg C to + 50 deg C

(b) Hughes: 0 deg C to + 30 deg C

Needs to be resolved.

TMI
Conceptual Design Review
August 25 - 27, 1992

SIGN-IN SHEET

26 AUG 92

NAME	ORGANIZATION	RESPONSIBILITY	MAIL STATION	PHONE
JANE LANGAN	NASA/GSFC	Program Analyst	153	301-286-6545
Kenne Buckhart	NASA/GSFC	Contracting Officer	284.7	301-286-8304
Mickelle Manni	NASA/GSFC	Financial Ingr	490	301-286-8199
DICK HARRINGTON	OLD DOMINION UN.	TECH ADVISORY GROUP		(804) 864-8472
James SHIVE	NASA/GSFC	TMI instrument scientist	975	301-286-6716
TOM TOUTSI	NASA/GSFC	PERFORMANCE ASSURANCE	490	301-286-5444
Nes Lawrence	NASA/LaRC	Tech Advisory Group	490	(804) 864-1821
Grace Bell	NASA/GSFC	Resource Analyst	490	(301) 286-1386
Tom Wilheit	TEXAS A&M	RADIATION TEAM on P.S.T.	DEPT OF AERONAUTICS TAMU CS. TX 77843	(409) 845-0176
Tom Keating	NASA/GSFC	Systems Manager	490	301 286 7965
WALT MASEROWICZ	NASA/GSFC/CSC	SCHEDULE MANAGER	490	(301) 286-5622
Dorothy Pennington	NASA/GSFC	Dep. Project Mgr / Resources	490	301-286-4922
TOM LAVIGNA	NASA/GSFC	PROJECT MANAGER	490	301-286-8351
RICH LAWRENCE	NASA/GSFC	INSTRUMENT SYSTEMS MGR	490	301-286-1022
E LOBL	HAC	SSM/I	550/X322	(310) 416-4237
GARY WENGROW	HAC	PRODUCT ASSURANCE	552/K309	(810) 416-2593
Dick Lang	HAC	PRODUCT ASSURANCE	550/X331	(310) 416-4185
Bob Maichle	GSFC	system Engineering	704.1	301-286-5222
Ralph Viehman	GSFC	Performance Assurance	490	301-286-5817
SHARON COOPER	NASA/GSFC	MECHANICAL ENG.	722.2	301-286-9939
BRUCE DROED	HAC	Atomic Oxygen	541 / B300	(310) 364-8341
DICK ALLEN	HAC	CONFIGURATION/ DATA MANAGEMENT	550/X331	(310) 416-4242
Jay Vanthland	HAC	Deployment Mechanisms	E1/D151	(310) 416-5341
Pete Mavrodakis	HAC	SPIN CONTROL SYSTEM	E1/D110	(310) 416-5266

TMI
Conceptual Design Review
August 25 - 27, 1992

SIGN-IN SHEET

26 AUG 92

NAME	ORGANIZATION	RESPONSIBILITY	MAIL STATION	PHONE
Umesh Ketkar	HAC	Mechanisms/Controls	E1/D151	416-5348
JOHN STICKELMAIER	HAC	REA POWER SUPPLY	S12/W323	416-5071
TIM TRAYNOR	HAC	REA BAPTA MECHANISM	E1/D151	416-5336
TOM EAKINS	HAC	SCIENCE/APPLICATIONS PROGRAMS	S41/A324	416-3826
PAUL A. TOTH	HAC	RECEIVERS	S12/W325	416-5016
SAMUEL REYNOLDS	HAC	RECEIVERS	S12/W325	(610) 416-5013
MIKE CRAWFORD	HAC	SPL REA	S4/S309	364-9758
STEVE LINDSEY	HAC	SPL DESIGN	S4/S307	364-9515
JUDY EIDE	HAC	Facilitator (Product Assurance)	S52/K306	416-2584
CARL STAMMERJON	HAC	STRUCTURES/INTEGRATION	E1/D151	416-5349
HIRAM OHTA	HAC	ANTENNA	S12/W319	416-6062
Doug Purinton	HAC	Thermal	S41/B300	364-8297
Yi-Chi Shih	HAC	Receiver	S12/W327	364-5116
Victor Reinhardt	HAC	Receiver/ Power Supply	S12/W325	416-4980
Dave Sirota	HAC	Test Pgm Mgr	SC/S50/X331	310 416-4173
JEFF WEILS	HAC	BVS MGR	SC/S50/X322	310-416-5354
JOE THOMAS	HAC	REC, ANT, PS	SC/S40/T336	310-416-6040
KHANH V. TS	HAC	ANTENNA	SC/S12/V347	310-416-2070
Jim Prince	HAC	PROGRAM MAN.	SC/S50/X322	310 416 3365
Jim Felicita	HAC	Contracts	SC/S50/X331	310-416-4244
ARISTEO PEREZ	HAC	THERMAL	SC/S07/G302	364-9489